Published in final edited form as:

Nat Cell Biol. 2022 May ; 24(5): 793–804. doi:10.1038/s41556-022-00893-0.

Cancer-cell-secreted miR-122 suppresses *O*-GlcNAcylation to promote skeletal muscle proteolysis

Wei Yan[1,*], **Minghui Cao**[1], **Xianhui Ruan**[1], **Li Jiang**[1], **Sylvia Lee**[2], **Adriana Lemanek**[2], **Majid Ghassemian**[3], **Donald P. Pizzo**[1], **Yuhao Wan**[1], **Yueqing Qiao**[1], **Andrew R. Chin**[1], **Erika Duggan**[4], **Dong Wang**[5], **John P. Nolan**[4], **Jeffrey D. Esko**[6,7], **Simon Schenk**[2,*], **Shizhen Emily Wang**[1,8,*]

[1]Department of Pathology; University of California, San Diego; La Jolla, CA 92093; USA

[2]Department of Orthopaedic Surgery; University of California, San Diego; La Jolla, CA 92093; USA

[3]Biomolecular and Proteomics Mass Spectrometry Facility; University of California, San Diego; La Jolla, CA 92093; USA

[4]Scintillon Institute; San Diego, CA 92121; USA

[5]Skaggs School of Pharmacy and Pharmaceutical Sciences; University of California, San Diego; La Jolla, CA 92093; USA

[6]Department of Cellular and Molecular Medicine; University of California, San Diego; La Jolla, CA 92093; USA

[7]Glycobiology Research and Training Center; University of California, San Diego; La Jolla, CA 92093; USA

[8]Moores Cancer Center; University of California, San Diego; La Jolla, CA 92093; USA

Abstract

A decline in skeletal muscle mass and lower muscular strength are prognostic factors in advanced human cancers. Here, we found that breast cancer suppressed *O*-linked *N*-acetylglucosamine (*O*-GlcNAc) protein modification in muscle through extracellular-vesicle-encapsulated miR-122,

*Correspondence should be addressed to SEW, SS, and WY. S. Emily Wang (emilywang@ucsd.edu) – Lead Contact, Department of Pathology; University of California, San Diego, 9500 Gilman Drive; La Jolla, California 92093-0612; USA, Tel: 01-858-246-2464, Simon Schenk (sschenk@ucsd.edu), Department of Orthopaedic Surgery; University of California, San Diego, 9500 Gilman Drive; La Jolla, California 92093-0863; USA, Tel: 01-858-822-0857, Wei Yan (yanweisibs@gmail.com), Department of Pathology; University of California, San Diego, 9500 Gilman Drive; La Jolla, California 92093-0612; USA, Tel: 01-858-246-2464.

Author Contributions Statement

S.E.W., S.S., and W.Y. conceived ideas. S.E.W., S.S., W.Y., and J.D.E. contributed to project planning and manuscript writing. W.Y. and S.E.W. designed and performed most of the experiments. S.L., A.L., and S.S. performed muscle mechanics tests and analyses. M.G. assisted with mass spectrometry analysis. M.C. and A.R.C. assisted with cell line construction. M.C., X.R., L.J., and Y.W. assisted with mouse experiments. Y.Q. assisted with data analysis. E.D. and J.P.N. performed EV characterization by flow cytometry. D.P.P. assisted with tissue processing and histological analyses. D.W. contributed to characterization of RYR1 PTMs and functional domains.

Competing Interests Statement

The authors declare no competing interests.

which targets *O*-GlcNAc transferase (OGT). Mechanistically, *O*-GlcNAcylation of the ryanodine receptor 1 (RYR1) competed with NEK10-mediated phosphorylation and increased K48-linked ubiquitination and proteasomal degradation; the miR-122-mediated decrease in OGT resulted in increased RYR1 abundance. We further found that muscular protein *O*-GlcNAcylation was regulated by hypoxia and lactate through HIF1A-dependent OGT promoter activation and was elevated after exercise. Suppressed *O*-GlcNAcylation in the setting of cancer, through increasing RYR1, led to higher cytosolic Ca^{2+} and calpain protease activation, which triggered cleavage of desmin filaments and myofibrillar destruction. This was associated with reduced skeletal muscle mass and contractility in tumour-bearing mice. Our findings link *O*-GlcNAcylation to muscular protein homeostasis and contractility and reveal a mechanism of cancer-associated muscle dysregulation.

Keywords

Breast cancer; Extracellular vesicles; Cachexia; Skeletal muscle; Atrophy; Contractility; Calcium channel; *O*-GlcNAcylation

Introduction

Cancer exerts systemic effects partially through secreting extracellular vesicles (EVs) that can travel through the circulation and deliver bioactive cargo including miRNAs and proteins to various organs[1–3]. In addition to reprogramming cells in the tumour microenvironment and in a metastatic niche to promote tumour growth, immune evasion, and metastasis[4, 5], cancer-cell-secreted EVs can influence distant organs, including skeletal muscle, a tissue that is not usually colonized by cancer cells[6, 7]. A devastating cancer-associated effect is cachexia, a multi-organ energy-wasting syndrome presenting as substantial weight loss (primarily from muscle and body fat) and systemic inflammation[8, 9]. In breast cancer (BC), the most commonly diagnosed female cancer[10], the incidence of cachexia is ~19–40%[9, 11]. No widely approved drug is available to treat cancer cachexia, with current therapies non-specifically targeting systemic inflammation, energy intake, and physical activity[8].

Muscle proteolysis and atrophy is central to cachexia and may support tumour growth through the large release of amino acids into the circulation[9, 12]. The prevalence of low muscle mass and poor muscle quality is over one-third in non-metastatic BC patients at diagnosis[13], and nearly two-thirds in metastatic BC patients[14]; significantly, BC patients with reduced muscle mass have a greater risk of death compared to patients without[13, 15–17]. A net decline in total muscle protein underlies muscle atrophy, with this occurring via increased protein degradation and/or decreased synthesis. Activation of intracellular proteolytic systems has been widely demonstrated in muscle atrophy[18, 19]. Ca^{2+}-regulated cysteine proteases, calpains, mediate cleavage and depolymerization of desmin filaments, whose integrity is required for maintaining sarcomere architecture and myofibrillar stability[20]. The ubiquitin-proteasome system (UPS)-mediated myofibrillar destruction occurs subsequently upon dissociation of the desmin cytoskeleton, eventually resulting in muscle protein breakdown[20, 21]. Ca^{2+} influx through Ca^{2+} leak channels causes

Ca^{2+} binding and activation of calpains, increasing the rate of Ca^{2+}-dependent proteolysis in muscle atrophy[22].

Rapid Ca^{2+} release from the sarcoplasmic reticulum (SR) into the cytosol, and Ca^{2+} reuptake into SR is fundamental to muscle excitation-contraction (E-C) coupling and relaxation. Cytosolic [Ca^{2+}] is tightly regulated, with RYRs (RYR1 in skeletal muscle) being primary regulators of SR-Ca^{2+} release, and sarco/endoplasmic reticulum Ca^{2+}-ATPases (SERCAs) being key to cytosolic Ca^{2+} reuptake into SR[23, 24]. Mutations and post-translational modifications (PTMs) of RYR1, such as oxidation and nitrosylation, have been linked to severe muscle pathologies including muscular dystrophy and central core disease by inducing intracellular Ca^{2+} leak[25–29]. Bone-released TGF-β increases oxidization of RYR1 to cause muscle weakness, which only occurs in the setting of bone metastasis[26]. However, whether other PTMs also contribute to cancer-mediated muscle weakness, especially in BC, is unknown.

O-GlcNAcylation is a ubiquitous PTM that is controlled by OGT-mediated addition of a single GlcNAc moiety to the hydroxyl group of a specific serine or threonine residue in a target protein, and is removed by *O*-GlcNAcase (OGA/MGEA5)[30–32]. *O*-GlcNAcylation regulates protein complex formation and signal transduction partially through crosstalk with other common PTM codes, especially phosphorylation on the same Ser/Thr residues[30, 33]. The protein substrates of OGT are highly tissue-specific. Here we determined *O*-GlcNAcylated proteins in the skeletal muscles of tumour-free and tumour-bearing mice, identifying muscle proteins differentially modified in the presence of BC tumour as a mechanism mediating BC's systemic effect on skeletal muscle.

Results

BC-derived EV miR-122 suppresses *O*-GlcNAcylation in muscle

To confirm the *in vivo* uptake of BC-derived EVs by skeletal muscle, we engineered MDA-MB-231 BC cells and MCF-10A non-cancer mammary epithelial cells to stably express a membrane-targeted Lck-GFP[34]. EVs from both cell lines contained significant GFP labelling, with GFP^+ EVs uniformly distributed among total EVs in regard to particle size and surface tetraspanin expression (Extended Data Figure 1a). The GFP-labelled EVs were intravenously (i.v.) injected into female NOD/SCID/IL2Rγ-null (NSG) mice semi-weekly for 5 weeks before gastrocnemius (GA) was collected for fluorescent microscopy. In another experiment, MDA-MB-231/Lck-GFP cells were used to establish orthotopic xenograft tumours in the mammary fat pads. In both the EV injection model and xenograft tumour model, GFP was detected in a significant subset of muscle cells, indicating efficient uptake of administered or tumour-derived EVs (Figure 1a; Extended Data Figure 1b). Subcellular fractionation of GA from mice bearing MDA-MB-231/Lck-GFP tumours but not tumour-free mice indicated localization of GFP in the cytosolic compartment, confirming the internalization of EVs by muscle cells (Extended Data Figure 1c). Several EV protein markers, but not a Golgi marker, were detected in the EVs (Extended Data Figure 1d). Nanoparticle tracking analysis (NTA) and iodixanol density gradient ultracentrifugation confirmed the typical size, density, and protein expression of an exosome-enriched small EV (sEV) preparation (Extended Data Figure 1e–h).

We then performed RNA-seq on GA from mice injected with MCF-10A- or MDA-MB-231-derived EVs, which revealed differential gene expression associated with glycosaminoglycan metabolism, Ca^{2+} signalling, and muscle contraction (Figure 1b). The alteration in glycosaminoglycan metabolism led to our interest in protein glycosylation as a potential EV-mediated function, for which little knowledge is available. OGT transfers GlcNAc from UDP-GlcNAc to a target protein. Dysregulation of *O*-GlcNAcylation has been implicated in stress response, cancer, metabolic diseases, and neurological disorders[30–32]. Therefore, we focused on *O*-GlcNAcylation and its sole catalysing enzyme OGT. Significantly reduced OGT expression was observed in the skeletal muscle of mice receiving MDA-MB-231 BC-derived EVs compared with those receiving PBS or MCF-10A EVs (Figure 1c), and in mice bearing xenograft tumours compared with tumour-free controls (Figure 1d). To seek the potential mechanism leading to OGT downregulation, we searched for miRNAs with putative binding sites in the human *OGT* gene, and subsequently focused on miR-122–5p (miR-122), which is highly secreted by BC cells compared with non-cancer cells (Supplementary Table 1) and predicts metastasis in early-stage BC patients[35–37]. To determine the role of EV-encapsulated miR-122, we examined EVs from MCF-10A cells engineered to overexpress and secrete miR-122, which recapitulated the OGT-regulating effect, whereas EVs carrying miR-105 and serving as a control here failed to do so (Figure 1c). Density gradient ultracentrifugation confirmed co-enrichment of EV protein markers and miR-122 in EV fractions with a ~1.1–1.2 g/mL density (Extended Data Figure 1f,h). In contrast, MDA-MB-231 tumours with stable knockdown of Rab27a to suppress exosome secretion[38] or with miR-122 gene knockout failed to alter OGT expression (Figure 1d). Consistent with this, *O*-GlcNAcylation detected by *O*-GlcNAc antibodies was remarkably reduced in muscle from mice receiving high-miR-122 EVs or bearing tumours proficient in EV secretion and miR-122 expression compared to the corresponding control groups, whereas OGA/MGEA5 levels were not significantly affected (Figure 1e). Notably, no changes in *O*-GlcNAcylation were detected in lungs, liver, adipose tissue, kidney, and brain of tumour-bearing mice (Extended Data Figure 2a), and high-miR-105 EVs (as a control) had no effect on *O*-GlcNAcylation in the muscle (Extended Data Figure 2b).

We next performed mass spectrometry (MS) peptide identification using mouse GA protein extracts following *O*-GlcNAc enrichment to identity skeletal muscle proteins with *O*-GlcNAcylation. Among the identified peptides carrying HexNAc modifications (Supplementary Table 2), we focused on RYR1 and SERCA3, which were not detected from muscle of MDA-MB-231 tumour-bearing mice following *O*-GlcNAc enrichment. *O*-GlcNAcylation was identified on the T4338 residue in mouse RYR1 (equivalent to T4341 in human), which is conserved in primates and mouse, but replaced by an alanine in rat, rabbit, and other animals. For SERCA3, *O*-GlcNAcylation was identified on T534, which is conserved in human, mouse, and rat, but absent in SERCA1 and SERCA2 (Extended Data Figure 2c; Figure 1f). The identified *O*-GlcNAcylation sites were consistent with the computational predictions by OGTSite[39] (Extended Data Figure 2d).

O-GlcNAcylation regulates RYR1 ubiquitination and abundance

Skeletal muscle from mice receiving cancer EV treatment or carrying xenograft tumours, which showed suppressed OGT and *O*-GlcNAcylation, exhibited increased RYR1 and

decreased SERCA3 protein levels (Figure 1e). Overexpression of wild-type OGT, but not an enzymatic dead mutant (G482S) [40], decreased RYR1 and increased SERCA3 protein levels in C2C12 myotubes in a proteasome-dependent manner, whereas knockdown of OGT did the opposite (Figure 2a,b). Using ubiquitin mutants that only allow K48- or K63-linked polyubiquitination, we showed that RYR1 underwent K48-linked but not K63-linked polyubiquitination (Figure 2c), whereas SERCA3 was mainly modified by K63-linked polyubiquitination (Figure 2d). To further link protein ubiquitination and degradation to the herein identified *O*-GlcNAcylation events, we generated a T4341A mutant of human RYR1, in which the MS-identified *O*-GlcNAcylation site (equivalent to T4341 in human) is converted to alanine. To compare between wild-type RYR1 and the *O*-GlcNAcylation mutant, we expressed HA-tagged wild-type or mutant human RYR1 in C2C12 myotubes, where the exogenous RYR1 proteins showed colocalization with PDI, an endoplasmic reticulum marker (Extended Data Figure 3a). Overexpression of wild-type OGT decreased, whereas OGT knockdown increased, exogenously expressed wild-type RYR1 without affecting the T4341A mutant (Figure 2e,f). These effects were accompanied by corresponding changes in the ubiquitination level of wild-type RYR1 (Figure 2g,h). The herein identified *O*-GlcNAcylation site in RYR1 is also predicted by PhosphoSite [41] for potential phosphorylation on the same threonine, suggesting a competition between the two types of PTMs. We therefore employed MS again to identify PTMs on immunoprecipitated RYR1 using C2C12 myotubes with or without OGT knockdown, which discovered phosphorylation on RYR1 T4338 only with OGT knockdown (Extended Data Figure 3b, Supplementary Table 3). Scansite predicted members of NIMA-related kinase (NEK) family as the potential kinases mediating phosphorylation at this site (Extended Data Figure 3c). Knockdown of NEK10, but not other NEKs, expressed in C2C12 cells decreased RYR1 protein levels (Figure 2i). In addition, NEK10 co-immunoprecipitated with RYR1; NEK10 knockdown decreased Ser/Thr phosphorylation of endogenous RYR1, whereas OGT knockdown increased the Ser/Thr phosphorylation of exogenously expressed wild-type, but not T4341A mutant, RYR1 (Figure 2j,k). When NEK10 was knocked down, OGT knockdown no longer increased RYR1 proteins (Figure 2l). These results suggest that NEK10-mediated phosphorylation may compete with *O*-GlcNAcylation on the threonine to regulate RYR1 ubiquitination and degradation. A search for potential ubiquitination sites in RYR1 revealed three lysine residues located ~200 amino acids downstream of the *O*-GlcNAcylated/phosphorylated threonine that are reported to be ubiquitinated in human and mouse cell lines (Extended Data Figure 3d) [42].

We used a similar strategy to characterize the role of SERCA3 *O*-GlcNAcylation and found that overexpression of wild-type OGT increased, whereas OGT knockdown decreased, exogenously expressed wild-type SERCA3 without affecting the T534A mutant that has lost the *O*-GlcNAcylation site (Extended Data Figure 4a,b). In contrast to K48-linked polyubiquitination, K63-linked polyubiquitylation is known to regulate proteasome-independent signalling, but how it leads to increased SERCA3 protein abundance remains unknown. The T534 *O*-GlcNAcylation site of SERCA3 was not predicted to undergo phosphorylation, suggesting different mechanisms are used to link *O*-GlcNAcylation to ubiquitination. Because our subsequent study supports a role of RYR1 but not SERCA3 in

the regulation of cytosolic Ca^{2+} influx, we did not further investigate how *O*-GlcNAcylation regulates SERCA3 ubiquitylation and degradation.

EV-encapsulated miR-122 regulates RYR1 by targeting OGT

Interrogation of sequences near the 3'UTR of human and mouse OGT genes identified two miR-122 binding sites in human and one site in mouse (Figure 3a). Luciferase reporter assays comparing miR-122 responsiveness of wild-type and miR-122-site-mutated constructs confirmed direct targeting of OGT by miR-122 through the upstream site in human and the only predicted site in mouse (Figure 3b). Transfection of C2C12 myotubes with miR-122 mimic significantly suppressed OGT expression, leading to increased RYR1 and decreased SERCA3 protein levels in a proteasome-dependent manner (Figure 3c). C2C12 myotubes took up EVs with high efficiency (Extended Data Figure 5a). Treatment with high-miR-122 EVs or miR-122 mimic suppressed OGT and *O*-GlcNAcylation with corresponding upregulation of RYR1 and downregulation of SERCA3 in myotubes, which was only observed when the myotubes were cultured in the presence of lactate or under hypoxia (Figure 3d,e; Extended Data Figure 5b–e). Exogenous expression of OGT abolished these effects of miR-122 (Figure 3d,e), confirming OGT's mechanistic role. We further tested a panel of human and mouse BC cell lines, which all secreted higher levels of miR-122 compared to MCF-10A cells (Figure 3f). EVs from these BC cells, but not those from MCF-10A, all downregulated OGT and corresponding regulation of RYR1 and SERCA3 in myotubes (Figure 3g).

OGT expression is induced by lactate and hypoxia via HIF1A

Our results suggested that certain contextual factors are required for miR-122-mediated downregulation of OGT, which was detected *in vivo* in skeletal muscle and *in vitro* in the presence of lactate or hypoxia. A thorough search of human and mouse OGT promoters revealed hypoxia response elements (HREs), which indeed mediate the promoter's activation by hypoxia-inducible factor 1A (HIF1A), as mutation of the HREs (for human OGT, mainly HRE I) abolished responsiveness to a HIF1A construct carrying a double proline to alanine substitution (dPA) that prevents hydroxylation and ubiquitin-proteasomal degradation even under normoxia (Figure 4a). This degradation-resistant form of HIF1A (dPA) also increased endogenous expression of OGT with decreased RYR1 and increased SERCA3 proteins (Figure 4b). A low concentration (2 mM) of lactate potently induced HIF1A and OGT expression in myotubes (Figure 4c; Extended Data Figure 5f). The OGT-inducing effect of lactate depended on reactive oxygen species (ROS) induction (Figure 4d), and was not recapitulated by HCl-induced acidity (Extended Data Figure 5g,h). It further enhanced the effect of hypoxia, and was detected immediately after 2 h of lactate treatment as well as the next day after the 2-h treatment (Figure 4e). HIF1A knockdown abolished the OGT-inducing effect of lactate as well as the corresponding regulations of RYR1 and SERCA3 protein abundances (Figure 4f; Extended Data Figure 5i,j).

As exercise has been shown to increase HIF1A proteins in skeletal muscle [43] and significantly elevated lactate concentration in serum (Figure 4g), we determined the effects of exercise. Female C57BL/6J mice immediately following 1 h of high-intensity treadmill

running showed increased levels of HIF1A, OGT, and *O*-GlcNAcylation with decreased RYR1 and increased SERCA3 proteins, compared to sedentary mice (Figure 4h,i).

Cytosolic Ca^{2+} is regulated by the miR-122–OGT–RYR1 axis

Next, we determined how *O*-GlcNAcylation influences Ca^{2+} flux through the regulation of RYR1 and/or SERCA3. Overexpression of OGT in myotubes blocked 4-CmC-stimulated cytosolic Ca^{2+} influx (Figure 5a), whereas OGT knockdown increased both basal and stimulated [Ca^{2+}] (Figure 5b). Treatment with lactate and miR-122 mimic, which up- and downregulated OGT respectively, reflected the effects of corresponding OGT levels (Figure 5c,d). EVs high in miR-122 elevated cytosolic [Ca^{2+}] before and after stimulation, which was abolished by exogenous OGT (Figure 5e). To evaluate the individual effect of RYR1 and SERCA3, we first overexpressed human RYR1 in myotubes and observed RYR1-dose-dependent elevations in cytosolic [Ca^{2+}], especially upon 4-CmC stimulation (Figure 5f). In contrast, knockdown of SERCA3 did not significantly alter Ca^{2+} flux (Figure 5g).

miR-122 induces calpain activity and muscle protein cleavage

Higher cytosolic [Ca^{2+}] may lead to aberrant activation of calpain proteases. Indeed, C2C12 myotubes transfected with miR-122 mimic or treated with high-miR-122 EVs showed higher calpain activity (Figure 6a,b). These were accompanied by enhanced cleavage of desmin and vimentin (detected by blocking subsequent proteasomal degradation of fragmented proteins), which was abolished by a calpain protease inhibitor (Figure 6c). Using an adenine base editor (ABE)-mediated A•T to G•C base editing strategy [44] we introduced a T4338A mutation to the endogenous RYR1 expressed in C2C12 myotubes (Figure 6d). In contrast to their wild-type counterparts, C2C12 myotubes carrying sequencing-verified T4338A mutation failed to respond to the effects of high-miR-122 EVs on RYR1 protein level, Ca^{2+} flux, calpain activity, and protein cleavage (Figure 6e–g).

Consistent with the myotube model, skeletal muscle from mice receiving high-miR-122 EVs or bearing EV/miR-122-proficient BC tumours showed higher calpain activity (Figure 7a,b), decreased GA and TA mass (Figure 7c,d), increased cleavage of desmin and vimentin (Figure 7e), and decreased OGT and increased RYR1 proteins (Extended Data Figure 6a,b). In mice bearing MDA-MB-231 xenograft tumours, we assessed contractile function of extensor digitorum longus (EDL), which showed a significantly lower force at various stimulation frequencies (30–120 Hz), and lower max tetanic tension, as compared to tumour-free mice; remarkably, this impairment was prevented in mice bearing a comparable size of Rab27a KD tumours (deficient in EV secretion) (Figure 7f,g). Mice carrying EV/miR-122-proficient tumours also showed reduced muscle strength in hang wire tests (Figure 7h). These results indicate that BC tumours can impact the intrinsic force-generating capacity of skeletal muscle, and that this reduction is mediated by EV secretion. Using a 4T1 orthotopic tumour model, we observed similar EV- and miR-122-dependent effects on *O*-GlcNAcylation, RYR1 level, protein cleavage, and skeletal muscle mass in female BALB/c mice (Figure 7i,j). Consistent with the induction of OGT and reduction of RYR1 proteins by exercise, decreased calpain activity and substrate cleavage were observed in the skeletal muscle of mice following 1 h of treadmill running (Extended Data Figure 6c,d), suggesting a potentially protective mechanism.

Exogenous OGT alleviates BC-induced proteolysis in muscle

To determine to what degree BC tumours dysregulate skeletal muscle through OGT, we constructed adeno-associated virus 8 (AAV8) expressing mouse OGT cDNA and injected the AAV-OGT into GA and TA following BC tumour implantation, with AAV-GFP serving as a control. GFP signals were detected in skeletal muscle but not in other organs or xenograft tumour of AAV-GFP-injected mice (Extended Data Figure 7a,b). AAV-OGT effectively restored OGT and *O*-GlcNAcylation in skeletal muscle of tumour-bearing mice, decreased RYR1 and increased SERCA3, and reversed tumour-associated calpain activation and protein cleavage (Figure 8a–d). Meanwhile, GA and TA mass were increased upon OGT restoration (Figure 8e,f), along with trends of slightly increased body weight and slightly decreased tumour volume (Figure 8g,h). However, this was not sufficient to significantly alter running capacity (Figure 8i,j).

Discussion

Here we identified *O*-GlcNAcylation as an integral layer of regulation in EV-mediated systemic effect of cancer. This mechanism seems specific to skeletal muscle, at least in the breast tumour models tested, and was not seen in other organs such as brain, lungs, and liver, despite the fact that circulating EVs from BC cells can be taken up in these organs[35, 45, 46]. Rather, other tissue-specific regulatory mechanisms controlling levels of *O*-GlcNAcylation, such as regulation of OGT (or OGA) promoter by transcriptional factors (e.g., the HIF1A-mediated mechanism reported herein), may override the effect of EVs in these organs. In cancer, OGT responds to glucose fluctuations and regulates glucose metabolism and cancer cell survival[47–49]. Here, we identify OGT as a nodal point that is regulated by physiological (e.g., exercise) and pathological (e.g., cancer) factors to influence skeletal muscle homeostasis and function.

As the largest homo-tetrameric ion channel, each RYR1 protomer contains multiple distinct domains based on resolved crystal structure[28, 50], whereby the herein identified *O*-GlcNAcylation site (T4338 in mouse RYR1, equivalent to A4330 in rabbit RYR1) resides between the central domain and channel domain (Extended Data Figure 8a,b). This region contains several putative EF-hand domains, with A4330 and the equivalent threonine in mouse and human RYR1 located within the E alpha-helix of an EF hand based on secondary structure modelling (Extended Data Figure 8c). It is possible that *O*-GlcNAcylation or phosphorylation on this threonine induces a conformational change to regulate binding of RYR1 by an E3 ligase for ubiquitination. We think the likelihood of *O*-GlcNAcylation to regulate RYR1 Ca^{2+} binding is low, as this threonine is only partially conserved across species. However, an increased amount of RYR1 proteins may result in unfolded or misfolded channels, and contribute to dysregulated Ca^{2+} handling.

While we show here that *O*-GlcNAcylation regulates RYR1-mediated Ca^{2+} flux, intracellular Ca^{2+}, in turn, has been shown to influence *O*-GlcNAc signalling. In the liver, glucagon-induced Ca^{2+} signalling leads to phosphorylation and activation of OGT and the subsequent *O*-GlcNAcylation and activation of Ulk proteins to drive autophagy in response to starvation[51]. Another study shows that in ventricular cells, NAD^+ and activation of RYR, as well as SERCA inhibition, all attenuate glucose-deprivation-induced

O-GlcNAcylation and ER stress, suggesting a Ca^{2+}-dependent mechanism[52]. Therefore, it would be important to understand the potential feedback regulation of *O*-GlcNAcylation by Ca^{2+} signalling especially under nutrient deprivation. The two-pronged regulation of OGT expression by HIF1A-dependent promoter activation and miRNA-mediated downregulation allows various signals, such as hypoxia and lactate reflecting local or systemic metabolic state and miRNA-loaded EVs transferred across organs, to integrate in the real-time tuning of *O*-GlcNAcylation. Previous research has linked hypoxia and HIF1A to muscle atrophy through mTOR-dependent inhibition of protein synthesis and transient activation of proteolysis through OGT-independent mechanisms[53]. Therefore, the overall effect of hypoxia-driven signalling on skeletal muscle, especially in cancer patients, would be far beyond the regulation of OGT and may involve metabolic reprogramming, mitochondrial remodelling (including enhanced mitophagy), muscle fibre atrophy, and altered muscle fibre type[53]. Other cancer comorbidities, such as diabetes, stroke, and osteoporosis, may also exert direct or indirect (by impairing physical activity) effects on skeletal muscle, adding another layer of complexity. Moreover, earlier studies have established inflammatory factors such as tumor necrosis factor-α (TNF-α) and interleukin-6 (IL-6) as principal mediators of cancer-related muscle wasting and cachexia. The pro-inflammatory pathways activate components of UPS, such as muscle-specific E3 ubiquitin ligases, to increase muscle protein degradation[54]. How the herein identified mechanism interconnects with these known pathways in the dysregulation of skeletal muscle warrants further investigation.

The herein reported HIF1A-dependent induction of OGT may mediate the physiological regulation of *O*-GlcNAcylation in skeletal muscle. By increasing OGT and decreasing RYR1, acute exercise may limit cytosolic Ca^{2+} transport to protect muscle from prolonged activity which can cause tissue damage. It would be interesting to explore cancer's effect on skeletal muscle under different states of muscle activity, which is especially relevant as physical exercise is part of the current clinical management for cancer cachexia. Impaired *O*-GlcNAcylation has been implicated in neurodegeneration; several OGA inhibitors that can enhance *O*-GlcNAc modification of Tau show a neuroprotective effect and are in clinical trials for treating Alzheimer's disease[55]. These inhibitors to elevate *O*-GlcNAcylation, as well as selective calpain inhibitors such as ABT-957/Alicapistat[56], may alleviate the herein reported muscular effect of cancer-secreted EVs and warrant future investigations in the setting of cancer.

Methods

This research complies with all relevant ethical regulations; all animal experiments were approved by the institutional animal care and use committee at the University of California, San Diego. Key resource information can be found in Supplementary Table 4.

Cells and constructs

Cell lines used in this study were obtained from American Type Culture Collection (Manassas, VA) and cultured in the recommended media or as indicated. These include MDA-MB-231 (HTB-26), 4T1 (CRL-2539), SK-BR-3 (HTB-30), MCF-7 (HTB-22), E0771 (CRL-3461), MCF-10A (CRL-10317), C2C12 (CRL-1772), and L6 (CRL-1458). MCF-10A

engineered to stably overexpress miR-122 (10A/miR-122) or the empty pBABE vector (10A/vec), as well as MDA-MB-231/Rab27a KD cells were constructed and cultured as previously described [35, 38]. Patient-derived BC cells PDX265922 (propagated in NSG mice and denoted as PDX) were derived from a triple-negative breast tumour as previously described [57] and cultured in Iscove's Modified Dulbecco's medium (Thermo Fisher Scientific; Waltham, MA) supplemented with 20% fetal bovine serum (FBS). C2C12 and L6 myoblasts were cultured in Dulbecco's Modified Eagle's medium supplemented with 10% FBS, which was changed to 2% FBS (for C2C12) or horse serum (for L6) for myotube differentiation of 4–7 days. When indicated, the myoblasts were cultured under 1% O_2 in an OxyCycler C42 Oxygen CO_2 Single Chamber (BioSpherix, Ltd.). Transient transfections of myoblasts were performed immediately after plating freshly trypsinized cells using X-tremeGENE™ HP DNA Transfection Reagent (Sigma-Aldrich, Cat# 6366244001) for DNA and Lipofectamine™ RNAiMAX Transfection Reagent (Thermo Fisher Scientific, Cat# 13778150) for RNA. Twenty-four h later, cells were switched to differentiation media. MDA-MB-231/Lck-GFP and MCF-10A/Lck-GFP cells were constructed by transfection of an Lck-GFP expression plasmid (Addgene plasmid # 61099) into MDA-MB-231 and MCF-10A cells followed by selection in G418 and sorting of GFP^+ cells by FACS. To construct 4T1/Rab27a KD cells, shRNA targeting Rab27a sequence CCAGTACACTGATGGCAAGTT was designed by BLOCK-iT™ RNAi Designer (Thermo Fisher Scientific) and the corresponding oligonucleotides were cloned into pLKO.1 vector (Addgene plasmid # 10878). Cells were transduced by the lentivirus and selected in puromycin. MDA-MB-231/miR-122 KO cells were constructed using CRISPR-Cas9 genomic editing system. Two single guide RNAs (DNA sequences CACACTAAATAGCTACTGCT and CACACTCCACAGCTCTGCTA) predicted by the sgRNA Designer (https://portals.broadinstitute.org/gpp/public/analysis-tools/sgrna-design) were synthesized in DNA form and annealed into double strands, treated with T4 polynucleotide kinase, and inserted into the BbsI-digested pSpCas9(BB)-2A-GFP vector [58]. The two constructs were co-transfected into MDA-MB-231 cells, and GFP^+ cells were sorted by FACS 24 h after transfection. A similar strategy was used to construct 4T1/miR-122 KO cells using two sgRNAs (DNA sequences TGTATGATGTGGTTTGTAAG and TTAGCCCTGAATCCAGCAGG). Monoclones were screened by genotyping PCR and confirmed by sequencing. For targeted T4338A mutagenesis of endogenous Ryr1, we used an adenine base editor (ABE)-mediated A•T to G•C base editing strategy [44] enabled by pCMV-ABE7.10-P2A-GFP plasmid (Addgene plasmid # 162509) [59] in combination with a sgRNA (target DNA sequence GGTG**A**CCCGCGCGGGGGGCG) predicted by Horizon CRISPR Design Tool (https://horizondiscovery.com/en/ordering-and-calculation-tools/crispr-design-tool) and cloned into pRG2 vector (Addgene plasmid # 104174) [60]. C2C12 cells were co-transfected by plasmids carrying ABE and sgRNA at ~70% confluency. Singular GFP^+ cells were sorted by FACS 48 h later and seeded on 96-well plates (Corning; Corning, NY). Clones carrying the expected mutation were selected by targeted sequencing of a PCR-amplified region (PCR primers 5'-GCATCCTGGAGTACTTCCGGCCTTA [also used as the sequencing primer] and 5'-GGGCTCCACTGGCGTCGTGTCA). To construct AAV-OGT, the eGFP region in pscAAV-CMV-eGFP plasmid [61] were replaced with a DNA fragment containing mouse OGT cDNA, which was PCR-generated

using primers 5’-GTCAAGCTTACCATGCCGTCTTCCGTGGGCAACGTG and 5’-TTCGTTAACTCAGGCTGACTCGGTGACTTCAACA. The resulting construct pscAAV-CMV-mOGT was confirmed by sequencing. AAV serotype 8 was used to achieve robust transgene expression in skeletal muscle. Viruses were produced by the Vector Development Core Laboratory at UC San Diego, and titer was determined by PCR. For mouse injection, 5×10^{11} genome copy resuspended in 100 μl PBS was used. To construct reporters for miR-122-mediated regulation of OGT, a region encompassing partial coding region and 3’UTR of human *OGT* gene (primers 5’-AATCTCGAGTGCCCCAGAACCGTATCAT and 5’-ATTGCGGCCGCCAAACCAAACAGCAGTGCAG) and the 3’UTR of mouse *Ogt* gene (primers 5’-AAACTCGAGGGACCTTGCTGGTGTAGTCT and 5’-ATTGCGGCCGCCATCCCTATAGGAGGAATG) were cloned by PCR and inserted into the XhoI/NotI sites of psiCHECK-2 reporter vector (Promega) downstream of the *Renilla* luciferase (Rluc) gene. Site-directed mutagenesis was used to mutate the following putative miR-122 binding sites with corresponding primer sets: 5’-CCAAGCAGACATCAGCCAGCTGGCCTCTCCT and 5’-ACAGAGGACTCTGTAATGGGCACACCACAGGG for human site I; 5’-ACAGAGGTCTGGTGCCAAATGAAGATTTTTAG and 5’-TTAAAACACCCTAGGATGTTTTGAATCAGG for human site II; and 5’-CTAAGTGCAGTAGAGCAGTATAAACATACTCA and 5’-ACTGAGGACTCACAGATAAGTCTTGTCTGTT for mouse miR-122 site. The promoter region of human *OGT* gene was cloned from MCF-10A cells into pGL3-Basic reporter vector (Promega) using primers 5’-TCCAAGCTTGTGACAAAATGTCTGAACAGT and 5’-ATTGCGGCCGCAGCTTTCACAGGGCCAGTTG. Site-directed mutagenesis was used to mutate HRE I (primers 5’-TCGTCAAAATCCATGACTCTCCTCGAGTTG and 5’-AAAGAATCACCTTTAACATTTTTATGGCTGCCTT) and HRE II (primers 5’-CTAGATTGAGTCATGAATTGCCTCTACTTCCTT and 5’-AAAGTGGTTTAGGCAGATGGCAAGTGAATT). Site-directed mutagenesis was used to generate human $RYR1^{T4341A}$ mutant from a wild-type human RYR1 cDNA expression plasmid in pcDNA3.1(+) backbone [62] using primers 5’-CACTGCTGCCCAGAGCAGCGCCGCCACTGC and 5’-GCGCGCGCTGGGGCCGCTGGCGCGGGGGCG. GenBuilder™ Plus Cloning Kit (GenScript Biotech; Piscataway, NJ; Cat# L00744) was used to generate pcDNA3.1(+) expression plasmid of human RYR1 carrying an in-frame HA tag at the C terminus immediately before the stop codon of RYR1. To generate $SERCA3^{T534A}$ mutant, primers 5’-GCGGCTCCCCACGCGGACTGAGCTACAGCG and 5’-GCAGCACCCCTGACCCCCACCTCCAGGGAG were used to introduce the mutation into a wild-type human SERCA3 cDNA expression plasmid in pMT2 backbone (Addgene plasmid # 75189). An in-frame FLAG tag was inserted into the C terminus of wild-type or mutated SERCA3 using primers 5’-CTTTGTAGTCCTTCTGGCTCATTTCGTGCA and 5’-ACGATGACGACAAGTGAGCGCTGGGAACAGAG. All plasmid DNA were validated by sequencing.

Prediction of RYR1 modifications and secondary structure

O-GlcNAcylation of RYR1 and SERCA3 were predicted by OGTSite (http://csb.cse.yzu.edu.tw/OGTSite). Phosphorylation of RYR1 at T4341 was predicted by

PhosphositePlus (https://www.phosphosite.org/homeAction). Kinases that potentially phosphorylate this site were predicted by Scansite 4.0 (https://scansite4.mit.edu/4.0/#home). The secondary structure of selected RYR1 region was predicted by JPred 4 (http://www.compbio.dundee.ac.uk/jpred/).

EV purification and characterization

EVs were purified by ultracentrifugation of conditioned medium (CM) as previously described [35, 37, 63]. Briefly, CM was collected from cells grown in medium containing EV-depleted serum for 48 h, and pre-cleared by centrifugation at 500 g for 15 min and then at 12,500 g for 20 min. EVs were pelleted by ultracentrifugation at 110,000 g for 70 min, and washed in PBS using the same ultracentrifugation conditions. The EV pellet was suspended in PBS and used in various experiments. NTA was performed using a NanoSight NS300 (Malvern Panalytical). Iodixanol/OptiPrep density gradient centrifugation was performed as described [63]. For cell treatment, 2 μg of EVs (equivalent to those derived from ~5×10^6 producer cells) based on protein measurement using BCA protein assay kit (Thermo Fisher Scientific) were added to 2×10^5 recipient cells in a 6-well plate. For Ca^{2+} release assay, EV treatment was done in a 96-well plate with proportionally reduced EVs and cell numbers.

EV number, size and composition were determined by single vesicle flow cytometry [64] using a commercial assay kit (vFC™ Assay kit, Cellarcus Biosciences; San Diego, CA) and flow cytometer (CytoFlexS; Beckman Coulter, Indianapolis, IN). Briefly, samples were stained with the fluorogenic membrane stain vFRed™ and, where indicated, antibodies against CD9, CD63, and CD81-labeled with phycoerythrin (PE, Cellarcus Biosciences) for 1 h at RT, diluted 1000-fold in buffer, and measured using membrane fluorescence to trigger detection. Data were analysed using FCS Express, and included calibration using a vesicle size and fluorescence intensity standards. The analysis included a pre-stain dilution series to determine the optimal initial sample dilution and multiple positive and negative controls, as recommended by guidelines from the International Society for Extracellular Vesicles (ISEV) [65]. Details of vesicle flow cytometry can be found in Extended Data Figure 9, Supplementary Information, and Supplementary Table 5.

RNA extraction, reverse transcription, and quantitative PCR

These procedures were carried out as reported in [35, 37, 63]. Primers were designed using PrimerBank and the sequences are listed in Supplementary Table 4. An annealing temperature of 55°C was used for all primers. For mRNA detection, reverse transcription (RT) was performed using random primers and 18S rRNA was used as an internal reference in PCR to calculate the relative level of each mRNA. For miRNA detection, The U6 primer was used as an internal reference for intracellular miRNA levels. As a spike-in control for EV miRNA levels, 20 fmole of synthetic cel-miR-39–3p was added to EVs collected from equal number of cells during RNA extraction and its levels were subsequently used for data normalization in miScript miRNA RT-qPCR assays (Qiagen).

Western blots, immunoprecipitation (IP), and staining

Protein extracts were separated by electrophoresis on a 10% or 12% SDS polyacrylamide gel. Recipes of the lysis buffers were modified from Dr. Natasha Zachara lab's online protocol. Specifically, tissue lysis buffer contains 15 mM HEPES pH 7.3, 10% v/v glycerol, 0.5% v/v NP-40, 250 mM NaCl, 1 mM EDTA, and 10 μM PUGNAc with protease inhibitors and phosphatase inhibitors (Halt™ Phosphatase Inhibitor Cocktail; Thermo Fisher Scientific) added before use. Cell lysis buffer contains 20 mM Tris HCl pH 7.5, 150 mM NaCl, 1% v/v NP-40, 2 mM EDTA, and 10 μM PUGNAc with protease/phosphatase inhibitors added before use. Calpain protease activity was measured using Calpain Activity Fluorometric Assay Kit (Sigma-Aldrich, Cat# MAK228) following manufacturer's protocol. The same lysis buffer was used to prepare lysates for protein cleavage detection by Western blot. GAPDH was used as a loading control. IP of ubiquitinated proteins was performed in myotubes transfected with HA-tagged Ub-WT, Ub-K48, or Ub-K63 expression plasmid (Addgene plasmid # 17608, 17605, 17606) [66] or their MYC-tagged versions generated by replacing the HA-tag-containing EcoRI/SalI fragment with a sequence coding for 5xMYC-tag. For all IP, cell lysates were pre-cleared with control IgG and protein A agarose beads (Thermo Fisher, Cat# 20333) for 30 min prior to IP with the corresponding antibody and fresh protein A agarose beads for 2 h at 4 °C. Unprocessed original scans of all blots are shown in source data files. Muscle tissues were fixed in 10% neutral buffered formalin and embedded in paraffin for sectioning. Immunohistochemistry (IHC) was performed as previously described [35, 37, 63]. Stained slides were scanned using an Aperio VERSA digital pathology scanner (Leica Biosystems; Buffalo Grove, IL). Immunofluorescent staining of C2C12 myotubes was performed following a reported protocol [67]. Subcellular fractionation of skeletal muscle tissue was performed using a commercial kit (Thermo Fisher, Cat# 89874). All antibodies used in this study are listed in Supplementary Table 4.

Sample preparation and mass spectrometry

To identify proteins with *O*-GlcNAcylation modification, 10 mg of GA from tumour-free or MDA-MB-231 tumour-bearing mice were lysed in ice-cold tissue lysis buffer. Insoluble proteins were removed by centrifugation at 18,000 g for 10 min at 4 °C, and the supernatant was incubated overnight with CTD110.6 antibody conjugated to dynabeads (Dynabeads® antibody coupling kit; Thermo Fisher Scientific). The beads were washed in PBS and subjected to peptide digestion and MS. To characterize the PTMs of RYR1, C2C12 myotubes transfected with control siRNA or siOGT were lysed in the cell lysis buffer described above, and the protein extract was immunoprecipitated by RYR1 antibody conjugated to dynabeads. Proteins on the beads were separated by SDS-PAGE, bands on the gel were visualized by silver staining (SilverQuest™ silver staining kit; Thermo Fisher Scientific), and a region of gel containing proteins of >250 kDa was cut for in-gel digestion and MS. Proteins were digested and extracted from SDS-PAGE as described in [68]. Trypsin-digested peptides were analyzed by ultra-high pressure liquid chromatography (UPLC) coupled with tandem mass spectroscopy (LC-MS/MS) using nano-spray ionization. The nano-spray ionization experiments were performed using an Orbitrap fusion Lumos hybrid mass spectrometer (Thermo) interfaced with nano-scale reversed-phase UPLC (Thermo Dionex UltiMate™ 3000 RSLC nano system) using a 25-cm, 75-micron ID glass capillary packed with 1.7-μm C18 (130) BEHTM beads (Waters corporation). Peptides were eluted

from the C18 column into the mass spectrometer using a linear gradient (5–80%) of ACN (Acetonitrile) at a flow rate of 375 μl/min for 1 h. The buffers used to create the ACN gradient were: Buffer A (98% H_2O, 2% ACN, 0.1% formic acid) and Buffer B (100% ACN, 0.1% formic acid). Mass spectrometer parameters are as follows: an MS1 survey scan using the orbitrap detector (mass range [m/z]: 400–1500 using quadrupole isolation, 60000 resolution setting, spray voltage of 2400 V, Ion transfer tube temperature of 285 °C, AGC target of 400000, and maximum injection time of 50 ms) was followed by data-dependent scans (top speed for most intense ions, with charge state set to only include +2–5 ions, and 5 second exclusion time), while selecting ions with minimal intensities of 50000 at in which the collision event was carried out in A) high-energy collision cell (HCD Collision Energy of 30%), and the fragment masses were analysed in the ion trap mass analyser (with ion trap scan rate of turbo, first mass m/z was 100, AGC target 5000 and maximum injection time of 35 ms), followed by B) electron transfer dissociation (ETD Collision Energy of 25%, and EThcD setting active [SA Collision Energy of 25%]), and the fragment masses were analysed in the ion trap mass analyser (with ion trap scan rate of turbo, first mass m/z was 100, AGC target 5000 and maximum injection time of 35 ms). Data analysis was carried out using Byonic v3.8.13 (Protein Metrics Inc.).

Ca^{2+} release assay

Myotubes were washed once with 1× BSS buffer (140 mM NaCl, 2.8 mM KCl, 1 mM $MgCl_2$, 10 mM glucose, 2 mM $CaCl_2$, 10 mM HEPES, pH7.3) and loaded for 1 h in 2 μM Fura-2 AM (Life Technologies) and 0.02% pluronic F-127 (Sigma-Aldrich; St Louis, MO) at 37 °C in dark. Loaded cells were washed once with 1× BSS and once with 1× BSS containing 2 mM EGTA before Ca^{2+} release measurement was performed immediately using a Varioskan Lux luminescence spectrometer (Thermo Fisher). Fluorescence emission at 510 nm was used to determine the ratio of 340/380 nm excitation. To stimulate Ca^{2+} release, 4-chloro-m-cresol (4-CmC; Sigma Aldrich) was added at 500 μM.

Animals

All mice used in this study were obtained from the Jackson Laboratory. Female NOD/SCID/IL2Rγ-null (NSG) mice (for EV injection and MDA-MB-231 tumour models) or female BALB/c mice (for 4T1 tumour models) of ~8-week old were used in all studies except for muscle collection after exercise, where female C57BL/6J mice of ~15-week old were used. Mice were maintained in the University of California, San Diego Animal Care Program Facility under 12-hour light/12-hour dark cycle (on at 6:00 am/off at 6:00 pm) with temperature of 72 °F ± 2 and 30–70% humidity. EVs were injected into the tail vein semi-weekly for 5 weeks (~10 μg EVs per injection per mouse). MDA-MB-231 and 4T1 tumours were established by injecting 2×10^5 wild-type (control) cells, Rab27a KD cells, or miR-122 KO cells mixed with Matrigel (BD Biosciences) into the No.4 mammary fat pad. Tumour volume was calculated using the formula (length × $width^2$)/2. The maximal tumour size/burden permitted by the institutional animal care and use committee at the University of California, San Diego is a single mammary tumour reaching 1.5 cm in diameter. This maximal tumour size/burden was never exceeded in our mouse experiments. Lean body mass was determined by dual energy X-ray absorptiometry (DEXA) scan (PIXImus2; GE/Lunar, Madison, WI) and analysed using PIXImus software (2.10; GE/Lunar) at the end

of experiments. For OGT restoration in skeletal muscle, AAV8-OGT virus or control virus were injected into GA and TA of both sides (2.5×10^{10} genomic copy per injection per site) one week after implantation of MDA-MB-231 cells. For high-intensity treadmill running test, mice were acclimated to the treadmill 4–5 days prior to the exercise test session. The test was conducted on an open field six-lane treadmill (Eco 3/6; Columbus Instruments) set at a 10% incline. Following a 5-min 10 m/min acclimation period, the speed was increased by 2 m/min every 2 min to a maximal pace of 30 m/min until exhaustion [69]. Mice ran to exhaustion, defined as 10 consecutive seconds on the shock grid. Inverted screen test was performed as described [70] and hang time was recorded. For *ex vivo* muscle mechanics assessment, tetanic contractile function was assessed in the fifth toe muscle of the EDL as previously described [71, 72]. Muscle force was normalized to the muscle physiological cross-sectional area.

RNA-seq and GSEA

RNA sequencing and data analysis were carried out by Novogene (Sacramento, CA). RNA libraries were prepared for sequencing using standard Illumina protocols. mRNA was purified from total RNA using poly-T oligo-attached magnetic beads, and was fragmented randomly by addition of fragmentation buffer. Downstream analysis was performed using a combination of programs including STAR, HTseq, Cufflink and Novogene's wrapped scripts. Alignments were parsed using Tophat program and differential expressions were determined through DESeq2/edgeR. Reference genome and gene model annotation files were downloaded from genome website browser (NCBI/UCSC/Ensembl) directly. Indexes of the reference genome was built using STAR and paired-end clean reads were aligned to the reference genome using STAR (v2.5). STAR used the method of Maximal Mappable Prefix (MMP) which can generate a precise mapping result for junction reads. HTSeq v0.6.1 was used to count the read numbers mapped of each gene. And then FPKM (Fragments Per Kilobase Million) of each gene was calculated based on the length of the gene and reads count mapped to this gene. For GSEA, FPKM were uploaded to GSEA 4.2.0 and enrichment of gene sets was interrogated with 1,000 random permutations to obtain the normalized enrichment score (NES), nominal p-value, and false discovery rate (FDR) q-value.

Software

Equipment build-in software were used for data collection, including the CFX Manager Software version 2.0 for real-time PCR data and FCS Express version 7 (De Novo Software) for vesicle flow cytometry data. Prism 9 was used for most data analysis and statistics; Excel version 2112 was used for all t-tests; GSEA 4.2.0 was used for gene set enrichment analysis of RNA-seq data; ImageJ (1.53j) was used to quantify western blot data; Byonic v3.8.13 was used to analyse mass spectrometry-derived proteomic data; PyMOL (2.2) was used to display RYR1 structure; DIANA-TarBase v7 was used to predict miRNAs targeting *OGT*.

Statistics and reproducibility

All quantitative data are presented as mean ± standard error of mean (SEM). Unpaired two-tailed Student's t-tests were used for comparison of means of data between two groups. For multiple independent groups, one-way or two-way ANOVA with post hoc Tukey's or Bonferroni's multiple comparisons test were used. Values of $P<0.05$ were considered

significant. Sample size was generally chosen based on preliminary data indicating the variance within each group and the differences between groups. Except for RNA-seq and mass spectrometry, all experiments were performed at least twice independently with similar results. No samples or animals were excluded from the analysis. All mice/samples were randomized before experiments. Data collection and analysis were performed blinded to group allocation.

Data availability

The RNA-seq data that support the findings of this study have been deposited in the Gene Expression Omnibus (GEO) under accession codes GSE156909. Mass spectrometry data have been deposited in ProteomeXchange Consortium via the PRIDE [73] partner repository with the primary accession code PXD021232. The previously published GEO data set GSE50429 was reanalysed for miRNA levels in the cells and EVs of MDA-MB-231 and MCF-10A (Supplementary Table 1). The GSEA data in Figure 1b involved reanalyses of the Reactome pathway data sets R-HSA-1630316 and R-HSA-445355 as well as the KEGG (Kyoto Encyclopedia of Genes and Genomes) pathway data set hsa04020. All other data supporting the findings of this study are available from the corresponding author on reasonable request.

Extended Data

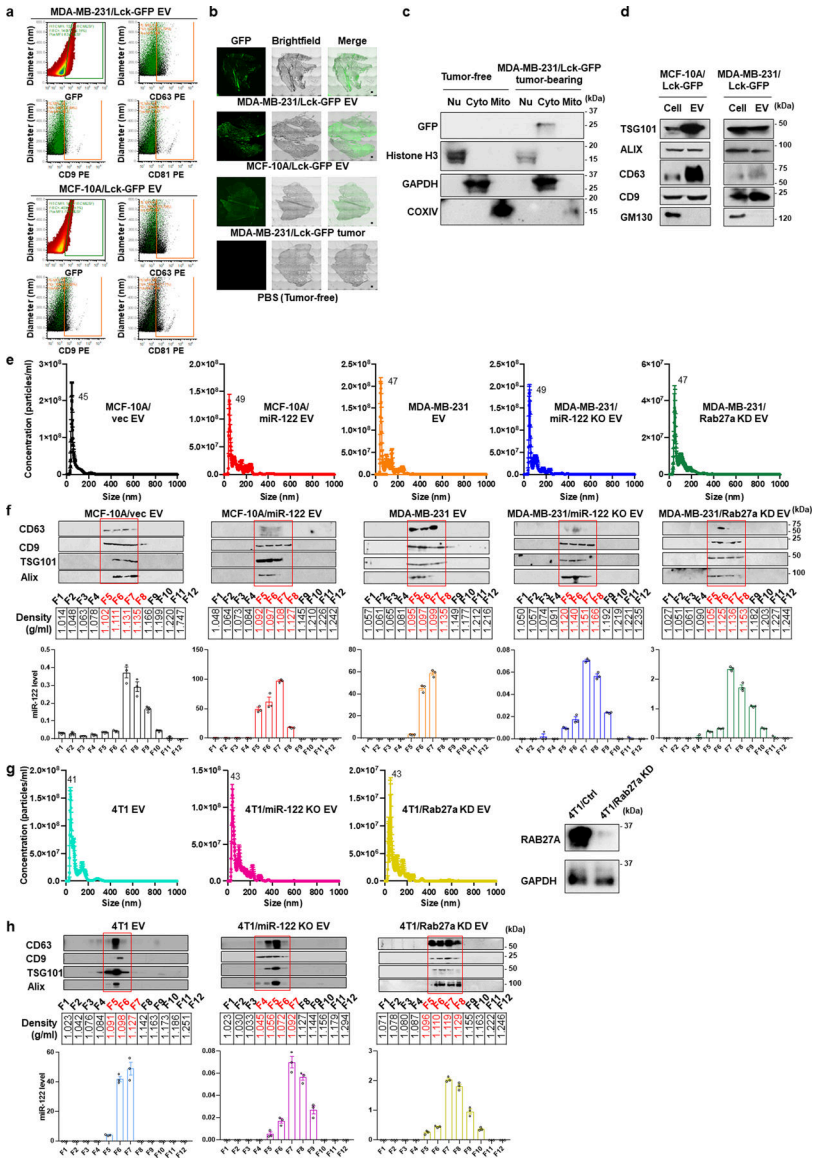

Extended Data Fig. 1. Characterization of EVs used in this study.

(a) Flow cytometry showing size distribution and expression of GFP and selected tetraspanins in EVs collected from MDA-MB-231/Lck-GFP and MCF-10A/Lck-GFP cells. GFP-positive EVs are displayed in green on dot plots of tetraspanin expression. **(b)** GFP fluorescence (green) in GA sections from NSG mice receiving tail vein injections of Lck-GFP-labelled EVs or bearing MDA-MB-231/Lck-GFP tumours. Scale bar=100 μm. **(c)** Western blots of nuclear, cytosolic, and mitochondrial fractions prepared from GA of tumour-free or MDA-MB-231/Lck-GFP-tumour-bearing mice showing the subcellular localization of GFP in the cytosol. Histone H3, GAPDH, and COXIV served as the markers for the nuclear, cytosolic, and mitochondrial fractions, respectively. **(d)** Western blots of indicated whole cell lysates and EVs showing EV markers and a Golgi marker (GM130, as a negative control for EV-specific proteins). **(e,g)** NTA of indicated EVs showing size

distribution (n=3 biological replicates). Western blots showing Rab27a knockdown in 4T1 cells were included next to the NTA in (g). **(f,h)** Levels of indicated EV proteins and RT-qPCR-determined miR-122 levels (normalized to a synthetic cel-miR-39–3p spike-in control added into each fraction) in OptiPrep gradient fractions (n=3 biological replicates). In bar graphs, values are shown as mean ± SEM. Unprocessed original scans of blots are shown in source data file.

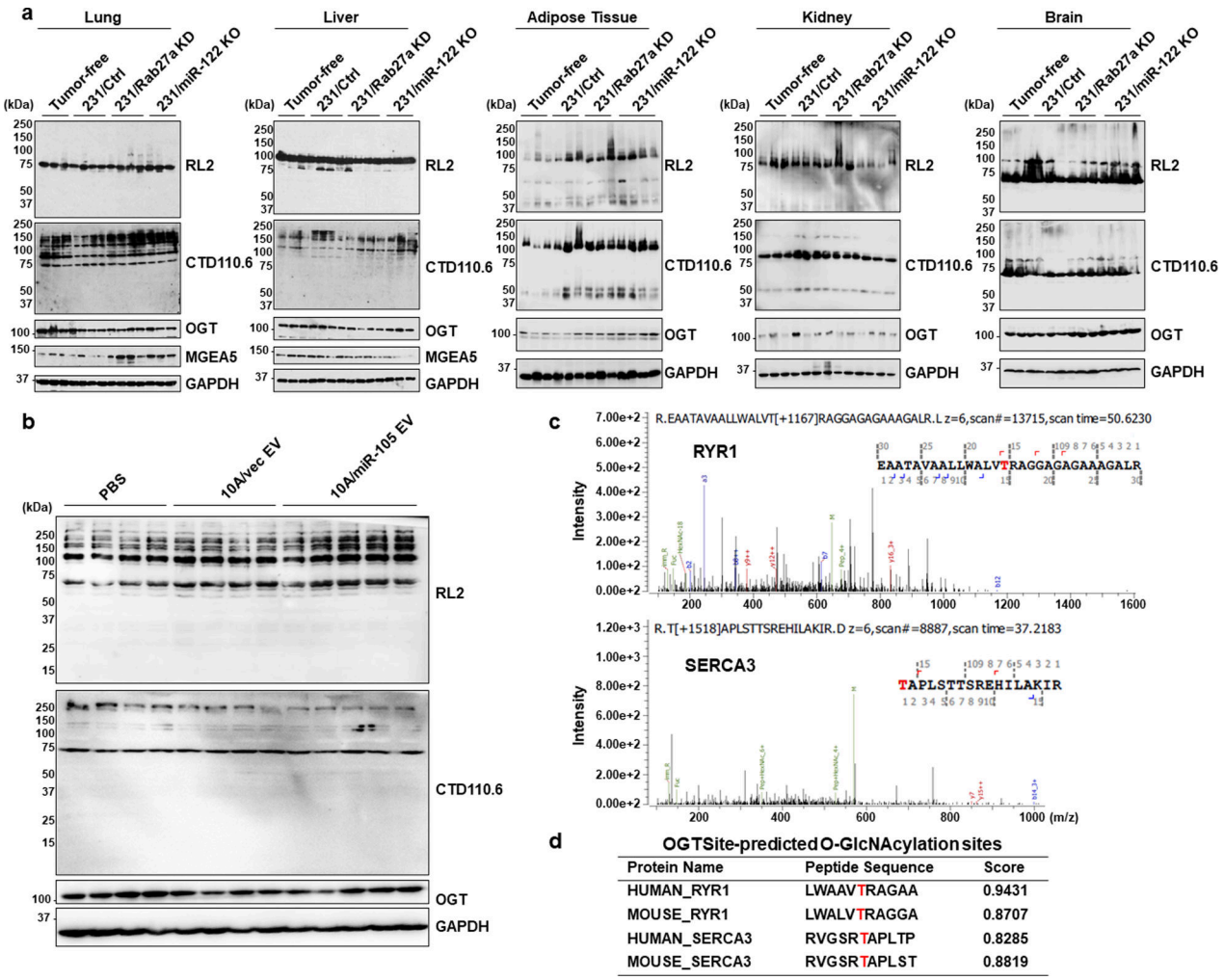

Protein Name	Peptide Sequence	Score
HUMAN_RYR1	LWAAVTRAGAA	0.9431
MOUSE_RYR1	LWALVTRAGGA	0.8707
HUMAN_SERCA3	RVGSRTAPLTP	0.8285
MOUSE_SERCA3	RVGSRTAPLST	0.8819

Extended Data Fig. 2. MS-identified *O*-GlcNAcylation of RYR1 and SERCA3 in skeletal muscle. **(a)** Western blots showing *O*-GlcNAcylation in lung, liver, adipose tissue, kidney, and brain of tumour-free and tumour-bearing mice described in Figure 1e. **(b)** Western blots of GA from mice that have received repeated injections of indicated EVs as in Figure 1e. **(c)** The MS/MS spectra of *O*-GlcNAcylated peptides of mouse RYR1 (residues 4324–4353) and SERCA3 (residues 534–550) with the triply charged precursor ion m/z 638.9881 (M + 3H)3+. The c- and z-type product ions were assigned. The *O*-GlcNAc oxonium ion (m/z, 204.09) and a series of its fragments (m/z, 186.08, 168.06, 138.05, and 126.05) were also assigned. **(d)** OGTSite analysis predicting the herein identified *O*-GlcNAcylation sites in RYR1 and SERCA3 of human and mouse.

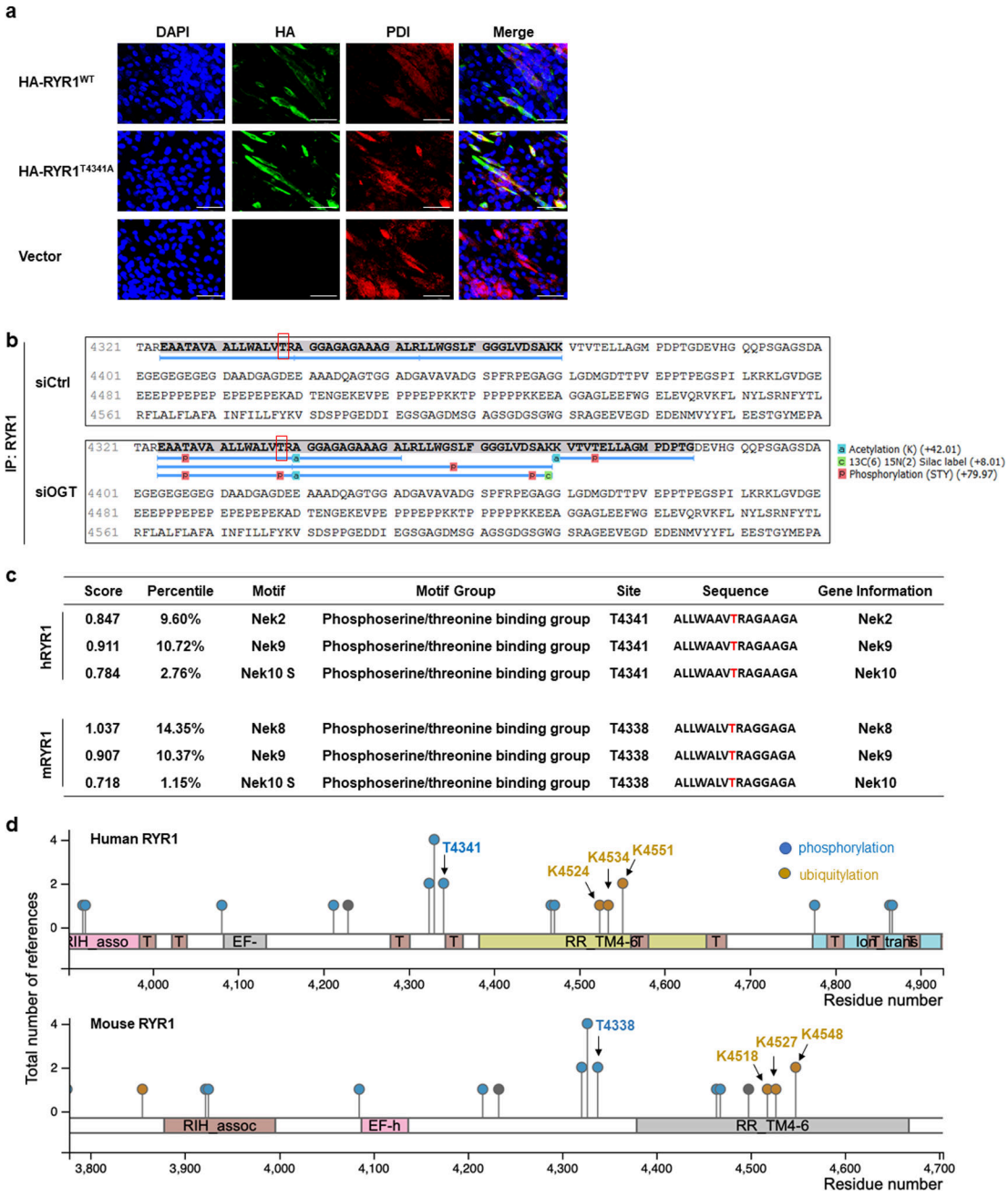

Extended Data Fig. 3. MS-identified RYR1 phosphorylation and the predicted kinases and nearby ubiquitylation sites.

(a) IF of C2C12 myotubes showing colocalization of exogenously expressed HA-tagged RYR1 and an ER marker PDI. DAPI stains the nuclei. Bar=100 μm. **(b)** MS-identified phosphorylation in immunoprecipitated, endogenous RYR1 from C2C12 with OGT knockdown but not from control C2C12. **(c)** Scansite 4.0 analysis predicting kinases that can potentially phosphorylate the identified threonine. **(d)** PhosphoSitePlus analysis showing published phosphorylation and ubiquitylation sites in the surrounding region in human and mouse RYR1.

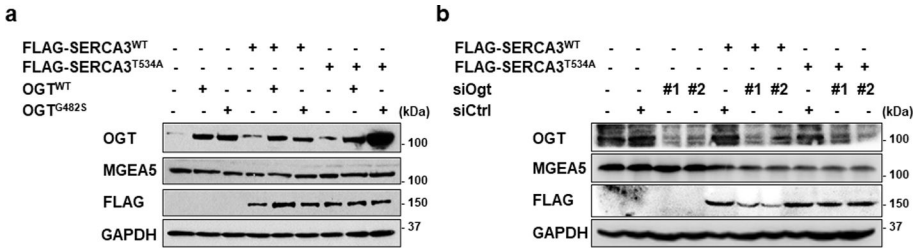

Extended Data Fig. 4. *O*-GlcNAcylation increases the abundance of SERCA3.

(a,b) C2C12 expressing FLAG-tagged wild-type SERCA3 or T534A mutant and with OGT overexpression (a) or knockdown (b) were analysed by western blots. Unprocessed original scans of blots are shown in source data file.

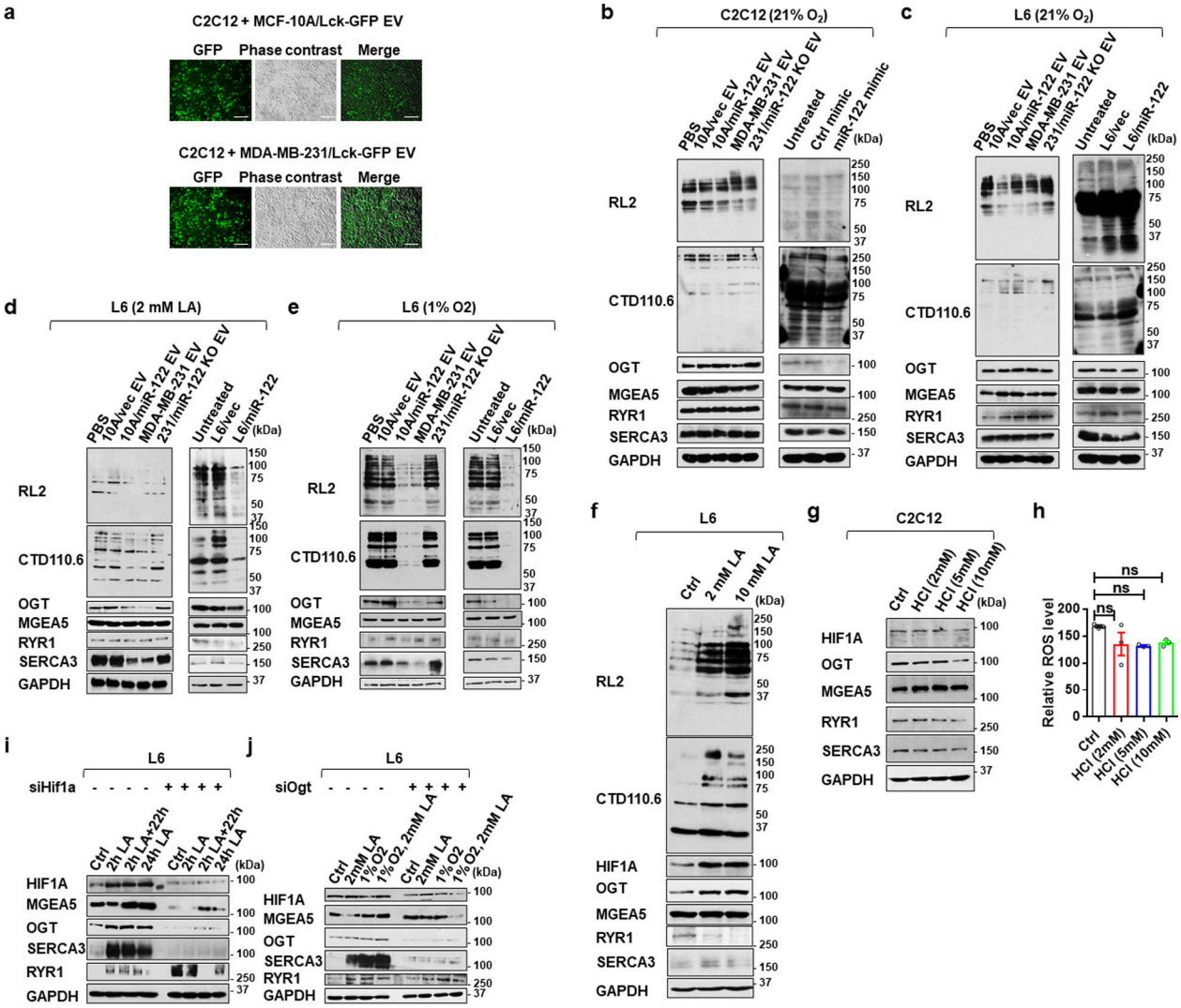

Extended Data Fig. 5. miR-122 regulates *O*-GlcNAcylation in myotubes in the presence of LA or under hypoxia in an HIF1A-dependent manner.

(a) GFP signals in C2C12 myotubes treated with indicated EVs for 24 h indicating EV uptake. Bar=100 μm. **(b,c)** Western blots showing indicated protein levels in treated C2C12

(b) and L6 myotubes (c) grown in the absence of LA and under 21% O_2. **(d,e)** Protein levels in L6 treated as indicated and grown in 2 mM LA (d) or under 1% O_2 (e). **(f)** Western blots showing indicated protein levels in L6 myotubes grown under indicated concentrations of LA for 24 h. **(g,h)** Protein levels (g) and ROS levels (h) in C2C12 myotubes treated with HCl to match the pH of indicated concentrations of LA (2mM: 2 mM LA). Values are shown as mean ± SEM in h (one-way ANOVA with Tukey's multiple comparisons test, n=3 biologically independent wells of cells). ns: not significant. **(i,j)** Protein levels in L6 treated with 2 mM LA (for 2 h, for 2 h followed by 22 h of incubation in LA-free medium, or for 24 h) and cultured under 21% or 1% O_2, and transfected with control siRNA or siRNA targeting HIF1A (i) or OGT (j), as indicated. Unprocessed original scans of blots are shown in source data file.

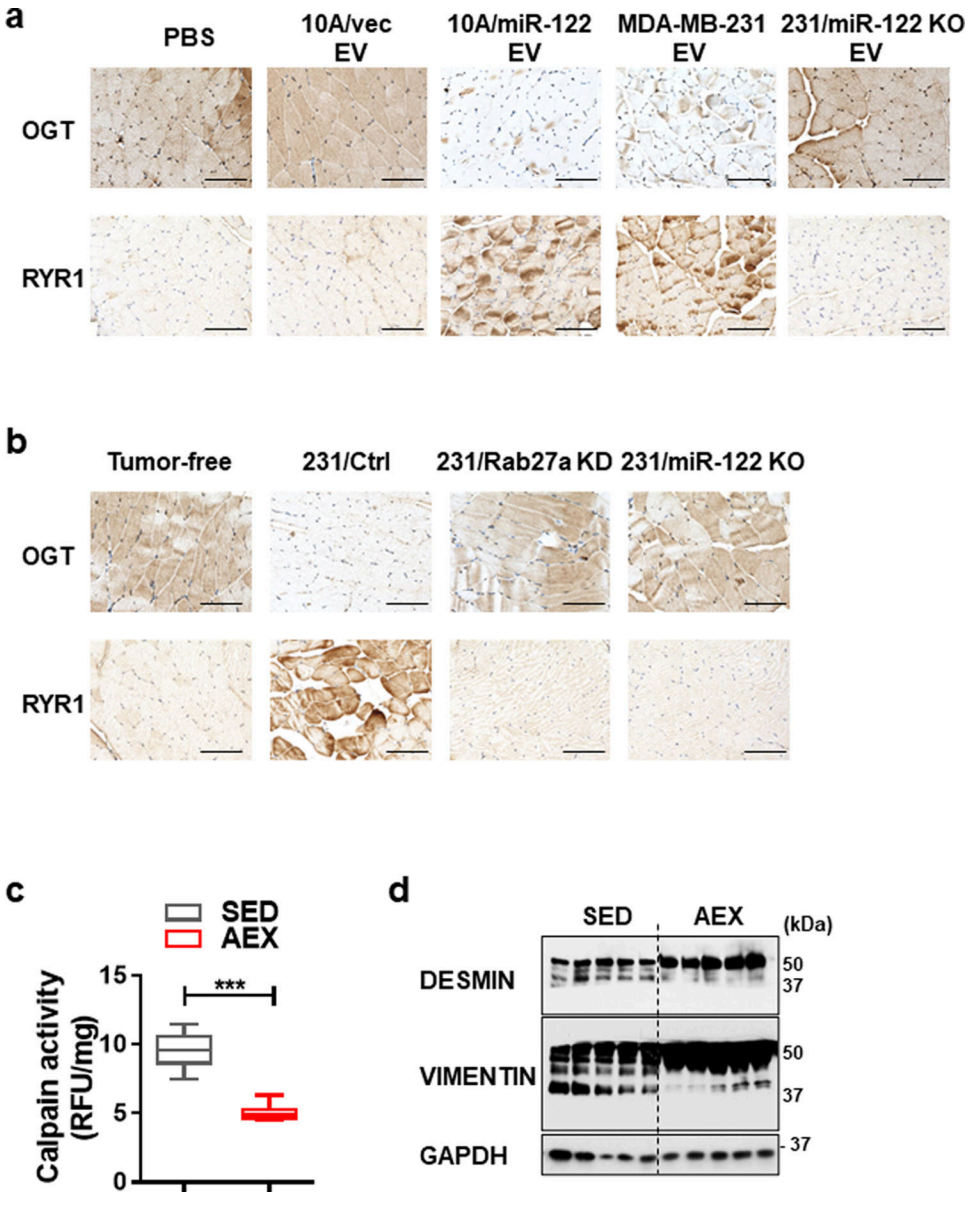

Extended Data Fig. 6. IHC of skeletal muscle and calpain activity assessments after aerobic exercise.

(a,b) IHC staining of GA from EV-treated (a) or tumour-bearing (b) mice. For tumour-bearing mice, muscle was analysed when tumours reached ~300 mm^3 in all groups. Bar=100 μm. **(c,d)** GA were collected from female C57BL/6J mice immediately after 1 h of high-intensity treadmill running (aerobic exercise/AEX) and from mice under sedentary lifestyle (SED). Tissue lysates were assessed for calpain protease activity (c; unpaired two-tailed t-test, n=6 mice per group) and by western blots for indicated protein cleavage (d). The boxes in the box-and-whiskers plot show the median (centre line) and the quartile range (25–75%), and the whiskers extend from the quartile to the minimum and maximum values. ***P<0.0001. Unprocessed original scans of blots are shown in source data file.

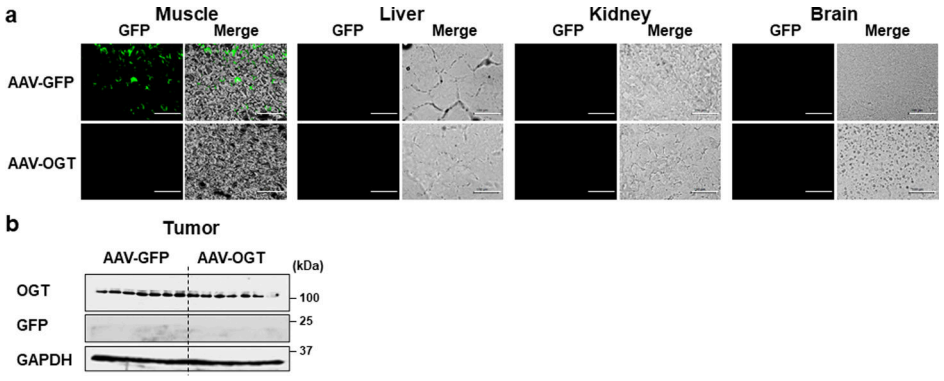

Extended Data Fig. 7. AAV-delivered gene expression in various organs.

(a) Fluorescent microscopy showing the presence or absence of GFP in various organs. Bar=100 μm. **(b)** Western blots of indicated tumour lysates from AAV-treated mice showing lack of GFP expression and lack of changes in OGT protein levels. Unprocessed original scans of blots are shown in source data file.

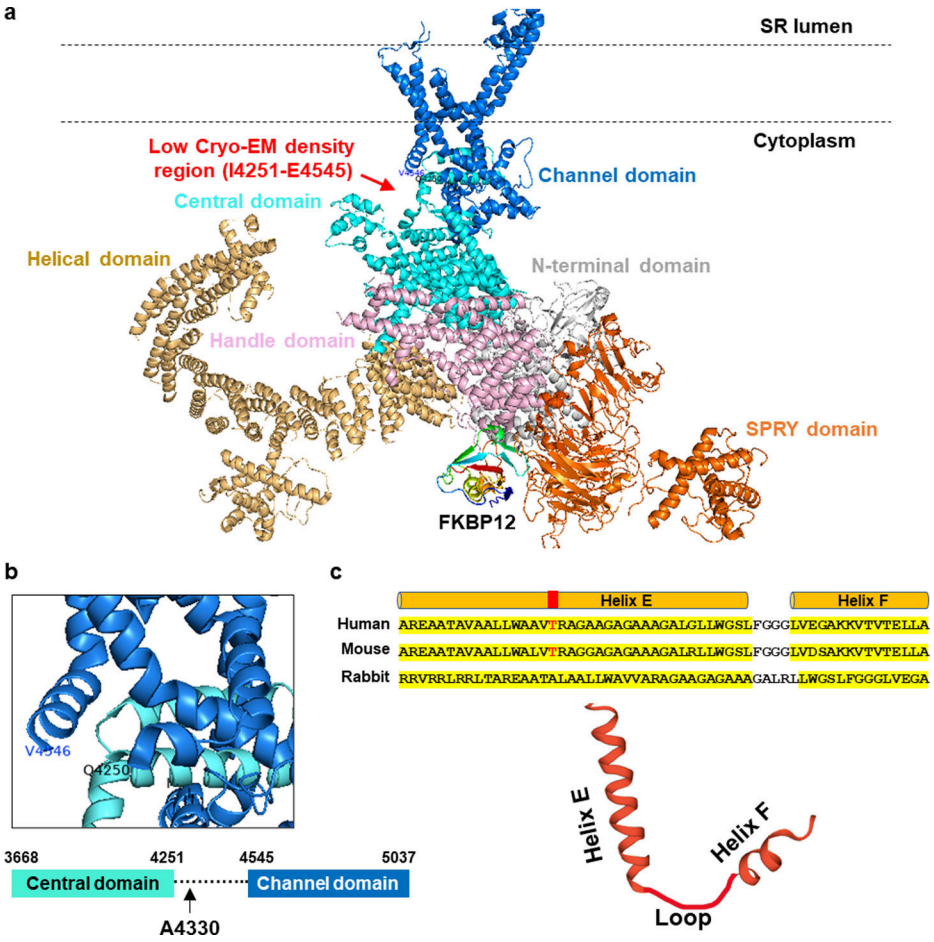

Extended Data Fig. 8. Structure of RYR1 monomer showing the *O*-GlcNAcylated threonine possibly residing in an EF-hand domain.

(a) Previously resolved structure of rabbit RYR1 monomer (PDB: 3J8H). Structure is displayed by PyMOL. **(b)** Partial structure showing the position of A4330 in rabbit RYR1 (equivalent to the *O*-GlcNAcylated threonine in human/mouse RYR1) within the linker region between central domain and channel domain. **(c)** JPred-predicted secondary structure of the peptide region with poor EM quality showing the *O*-GlcNAcylated threonine residing in the E alpha-helix of an EF hand.

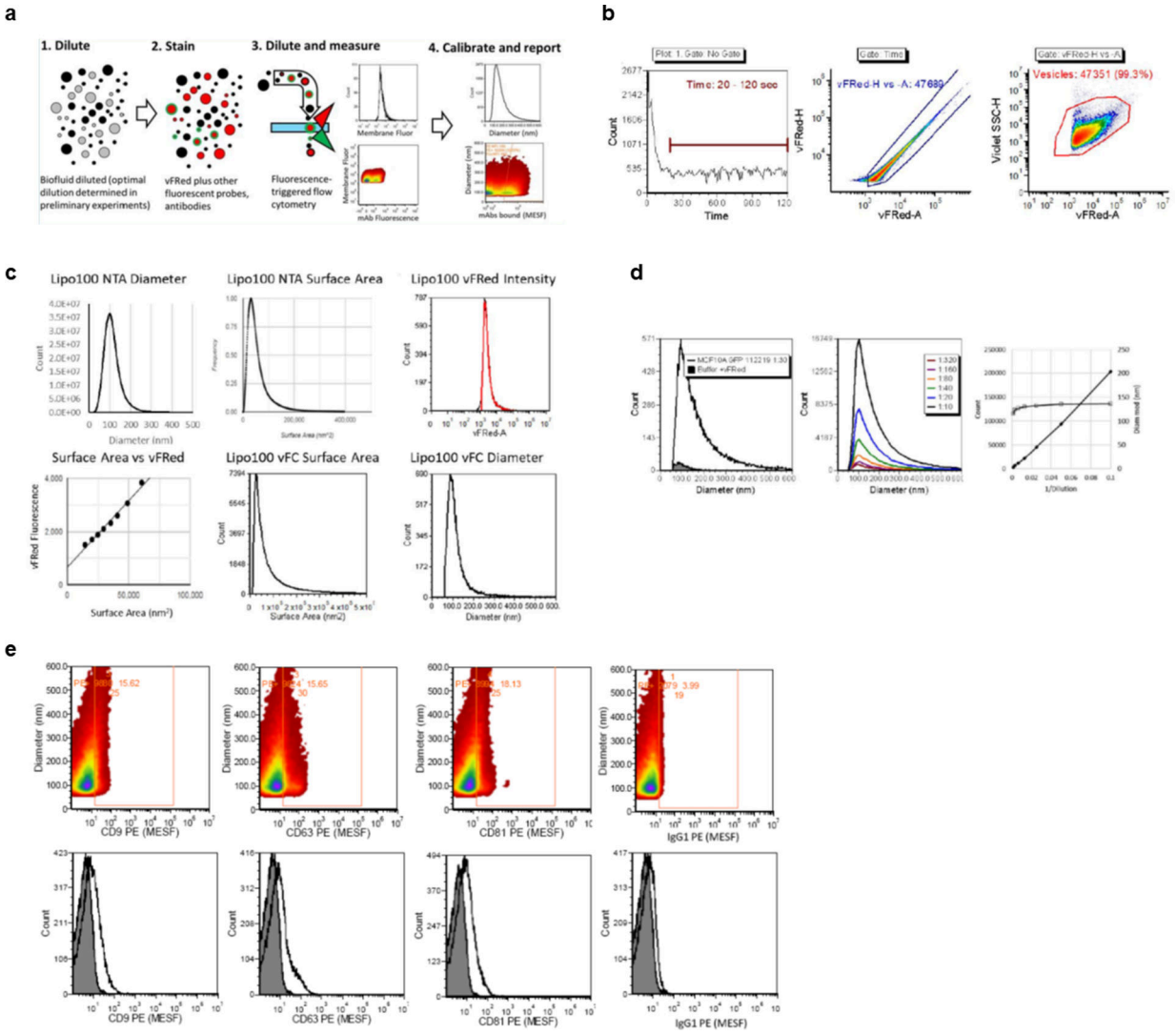

Extended Data Fig. 9. Method of vesicle flow cytometry (VFC).

(a) Schematic of VFC workflow. Vesicle flow cytometry (vFC™) is a homogeneous assay in which a cell-free sample, prepared by centrifugation, is stained with a fluorogenic membrane stain and one or more additional fluorescence probes then analysed by flow cytometry with detection triggered by membrane fluorescence. **(b)** VFC gating. Flow cytometry data is gated on time (left, to eliminate a fluidics-related background that occurs at the beginning of each sample measured in the CytoFlex), Membrane Stain fluorescence pulse height vs area (middle, vFRed-H v- A, which can help resolve EV-associated events from some sources of background), and by a gate (right, Vesicles) on Membrane fluorescence vs VSSC, which selects events with characteristic fluorescence and light scatter characteristics. **(c)** Vesicle size estimation. Vesicle size was estimated from the relationship between fluorescence intensity and vesicle surface area, as determined by the staining and analysis of a well-characterized synthetic vesicle size standard (Lipo100, Cellarcus Biosciences). The Lipo100 diameter distribution measured by NTA (upper left) was used to calculate the surface area distribution (upper middle), which, when compared to the

fluorescence intensity distribution after staining with vFRed (upper right), showed a linear relationship (lower left) that was used to convert the arbitrary vFRed fluorescence intensity into units of estimated equivalent surface area (lower middle) and diameter (lower right). **(d)** vFC Buffer +reagent and dilution controls. The single EV specificity of the measured marker positive events (left) was demonstrated by comparison to a Buffer +vFRed (no vesicle) sample and by serial dilution (middle) which demonstrated a ~2 log dynamic range (right) with no detectable coincidence/swarm. **(e)** Negligible Fc Receptor-mediated antibody binding as measured using an isotype-matched irrelevant control antibody. A representative EV sample immunostained with the indicated PE-labelled antibodies. MESF: mean equivalent soluble fluorochromes.

Supplementary Material

Refer to Web version on PubMed Central for supplementary material.

Acknowledgements

This work was supported by the National Institutes of Health (NIH) National Cancer Institute (NCI) grants R01CA218140 (SEW) and R01CA206911 (SEW), National Institute of Arthritis and Musculoskeletal and Skin Diseases (NIAMS) grant R21AR072882 (SS), and National Institute of General Medical Sciences (NIGMS) grant R01GM102362 (DW). Research reported in this publication included work performed in core facilities supported by the NIH NCI under grant numbers P30CA23100 (UC San Diego Cancer Center) and P30CA030199 (Sanford Burnham Prebys Cancer Center Flow Cytometry Core). We thank Dr. Michael C. Hogan for constructive suggestions, Dr. Antonio De Maio and his group for assistance with EV characterization by NTA, Dr. Xiaochun Yu for kindly providing the expression plasmids of wild-type and enzymatic dead (G482S) human OGT, Dr. Kathryn Stowell for kindly providing the pcDNA3.0-RYR1 expression plasmid, and Dr. Qing Zhang for kindly providing the expression plasmids of wild-type and dpA mutant of HIF1A.

References

1. Tkach M & Thery C Communication by Extracellular Vesicles: Where We Are and Where We Need to Go. Cell 164, 1226–1232 (2016). [PubMed: 26967288]
2. Becker A et al. Extracellular Vesicles in Cancer: Cell-to-Cell Mediators of Metastasis. Cancer Cell 30, 836–848 (2016). [PubMed: 27960084]
3. Redzic JS, Balaj L, van der Vos KE & Breakefield XO Extracellular RNA mediates and marks cancer progression. Semin Cancer Biol 28, 14–23 (2014). [PubMed: 24783980]
4. Wang SE Extracellular Vesicles and Metastasis. Cold Spring Harbor perspectives in medicine 10 (2020).
5. Sato S & Weaver AM Extracellular vesicles: important collaborators in cancer progression. Essays Biochem 62, 149–163 (2018). [PubMed: 29666212]
6. He WA et al. Microvesicles containing miRNAs promote muscle cell death in cancer cachexia via TLR7. Proc Natl Acad Sci U S A 111, 4525–4529 (2014). [PubMed: 24616506]
7. Zhang G et al. Tumor induces muscle wasting in mice through releasing extracellular Hsp70 and Hsp90. Nat Commun 8, 589 (2017). [PubMed: 28928431]
8. Fearon K, Arends J & Baracos V Understanding the mechanisms and treatment options in cancer cachexia. Nat Rev Clin Oncol 10, 90–99 (2013). [PubMed: 23207794]
9. Argiles JM, Busquets S, Stemmler B & Lopez-Soriano FJ Cancer cachexia: understanding the molecular basis. Nat Rev Cancer 14, 754–762 (2014). [PubMed: 25291291]
10. Siegel RL, Miller KD & Jemal A Cancer statistics, 2018. CA Cancer J Clin 68, 7–30 (2018). [PubMed: 29313949]
11. Fox KM, Brooks JM, Gandra SR, Markus R & Chiou CF Estimation of Cachexia among Cancer Patients Based on Four Definitions. J Oncol 2009, 693458 (2009). [PubMed: 19587829]

12. Fearon KC, Glass DJ & Guttridge DC Cancer cachexia: mediators, signaling, and metabolic pathways. Cell Metab 16, 153–166 (2012). [PubMed: 22795476]
13. Caan BJ et al. Association of Muscle and Adiposity Measured by Computed Tomography With Survival in Patients With Nonmetastatic Breast Cancer. JAMA Oncol 4, 798–804 (2018). [PubMed: 29621380]
14. Rier HN et al. Low muscle attenuation is a prognostic factor for survival in metastatic breast cancer patients treated with first line palliative chemotherapy. Breast 31, 9–15 (2017). [PubMed: 27810702]
15. Shachar SS et al. Skeletal Muscle Measures as Predictors of Toxicity, Hospitalization, and Survival in Patients with Metastatic Breast Cancer Receiving Taxane-Based Chemotherapy. Clin Cancer Res 23, 658–665 (2017). [PubMed: 27489287]
16. Prado CM et al. Sarcopenia as a determinant of chemotherapy toxicity and time to tumor progression in metastatic breast cancer patients receiving capecitabine treatment. Clin Cancer Res 15, 2920–2926 (2009). [PubMed: 19351764]
17. Villasenor A et al. Prevalence and prognostic effect of sarcopenia in breast cancer survivors: the HEAL Study. J Cancer Surviv 6, 398–406 (2012). [PubMed: 23054848]
18. Mueller TC, Bachmann J, Prokopchuk O, Friess H & Martignoni ME Molecular pathways leading to loss of skeletal muscle mass in cancer cachexia--can findings from animal models be translated to humans? BMC Cancer 16, 75 (2016). [PubMed: 26856534]
19. Sandri M Autophagy in skeletal muscle. FEBS Lett 584, 1411–1416 (2010). [PubMed: 20132819]
20. Aweida D, Rudesky I, Volodin A, Shimko E & Cohen S GSK3-beta promotes calpain-1-mediated desmin filament depolymerization and myofibril loss in atrophy. J Cell Biol 217, 3698–3714 (2018). [PubMed: 30061109]
21. Cohen S Role of calpains in promoting desmin filaments depolymerization and muscle atrophy. Biochim Biophys Acta Mol Cell Res 1867, 118788 (2020). [PubMed: 32603758]
22. Alderton JM & Steinhardt RA Calcium influx through calcium leak channels is responsible for the elevated levels of calcium-dependent proteolysis in dystrophic myotubes. J Biol Chem 275, 9452–9460 (2000). [PubMed: 10734092]
23. Lanner JT, Georgiou DK, Joshi AD & Hamilton SL Ryanodine receptors: structure, expression, molecular details, and function in calcium release. Cold Spring Harb Perspect Biol 2, a003996 (2010). [PubMed: 20961976]
24. Zalk R, Lehnart SE & Marks AR Modulation of the ryanodine receptor and intracellular calcium. Annu Rev Biochem 76, 367–385 (2007). [PubMed: 17506640]
25. Andersson DC et al. Ryanodine receptor oxidation causes intracellular calcium leak and muscle weakness in aging. Cell Metab 14, 196–207 (2011). [PubMed: 21803290]
26. Waning DL et al. Excess TGF-beta mediates muscle weakness associated with bone metastases in mice. Nat Med 21, 1262–1271 (2015). [PubMed: 26457758]
27. Bellinger AM et al. Hypernitrosylated ryanodine receptor calcium release channels are leaky in dystrophic muscle. Nat Med 15, 325–330 (2009). [PubMed: 19198614]
28. Zalk R et al. Structure of a mammalian ryanodine receptor. Nature 517, 44–49 (2015). [PubMed: 25470061]
29. Robinson R, Carpenter D, Shaw MA, Halsall J & Hopkins P Mutations in RYR1 in malignant hyperthermia and central core disease. Hum Mutat 27, 977–989 (2006). [PubMed: 16917943]
30. Yang X & Qian K Protein O-GlcNAcylation: emerging mechanisms and functions. Nat Rev Mol Cell Biol 18, 452–465 (2017). [PubMed: 28488703]
31. Hardiville S & Hart GW Nutrient regulation of signaling, transcription, and cell physiology by O-GlcNAcylation. Cell Metab 20, 208–213 (2014). [PubMed: 25100062]
32. Martinez MR, Dias TB, Natov PS & Zachara NE Stress-induced O-GlcNAcylation: an adaptive process of injured cells. Biochem Soc Trans 45, 237–249 (2017). [PubMed: 28202678]
33. Hart GW, Slawson C, Ramirez-Correa G & Lagerlof O Cross talk between O-GlcNAcylation and phosphorylation: roles in signaling, transcription, and chronic disease. Annu Rev Biochem 80, 825–858 (2011). [PubMed: 21391816]

34. Benediktsson AM, Schachtele SJ, Green SH & Dailey ME Ballistic labeling and dynamic imaging of astrocytes in organotypic hippocampal slice cultures. J Neurosci Methods 141, 41–53 (2005). [PubMed: 15585287]
35. Fong MY et al. Breast-cancer-secreted miR-122 reprograms glucose metabolism in premetastatic niche to promote metastasis. Nat Cell Biol 17, 183–194 (2015). [PubMed: 25621950]
36. Wu X et al. De novo sequencing of circulating miRNAs identifies novel markers predicting clinical outcome of locally advanced breast cancer. J Transl Med 10, 42 (2012). [PubMed: 22400902]
37. Zhou W et al. Cancer-Secreted miR-105 Destroys Vascular Endothelial Barriers to Promote Metastasis. Cancer Cell 25, 501–515 (2014). [PubMed: 24735924]
38. Shen M et al. Chemotherapy-Induced Extracellular Vesicle miRNAs Promote Breast Cancer Stemness by Targeting ONECUT2. Cancer Res 79, 3608–3621 (2019). [PubMed: 31118200]
39. Kao HJ et al. A two-layered machine learning method to identify protein O-GlcNAcylation sites with O-GlcNAc transferase substrate motifs. BMC Bioinformatics 16 Suppl 18, S10 (2015).
40. Chen Q, Chen Y, Bian C, Fujiki R & Yu X TET2 promotes histone O-GlcNAcylation during gene transcription. Nature 493, 561–564 (2013). [PubMed: 23222540]
41. Hornbeck PV, Chabra I, Kornhauser JM, Skrzypek E & Zhang B PhosphoSite: A bioinformatics resource dedicated to physiological protein phosphorylation. Proteomics 4, 1551–1561 (2004). [PubMed: 15174125]
42. Povlsen LK et al. Systems-wide analysis of ubiquitylation dynamics reveals a key role for PAF15 ubiquitylation in DNA-damage bypass. Nat Cell Biol 14, 1089–1098 (2012). [PubMed: 23000965]
43. Ameln H et al. Physiological activation of hypoxia inducible factor-1 in human skeletal muscle. FASEB J 19, 1009–1011 (2005). [PubMed: 15811877]
44. Gaudelli NM et al. Programmable base editing of A*T to G*C in genomic DNA without DNA cleavage. Nature 551, 464–471 (2017). [PubMed: 29160308]
45. Hoshino A et al. Tumour exosome integrins determine organotropic metastasis. Nature 527, 329–335 (2015). [PubMed: 26524530]
46. Chow A et al. Macrophage immunomodulation by breast cancer-derived exosomes requires Toll-like receptor 2-mediated activation of NF-kappaB. Scientific reports 4, 5750 (2014). [PubMed: 25034888]
47. Buren S et al. Regulation of OGT by URI in Response to Glucose Confers c-MYC-Dependent Survival Mechanisms. Cancer Cell 30, 290–307 (2016). [PubMed: 27505673]
48. Yi W et al. Phosphofructokinase 1 glycosylation regulates cell growth and metabolism. Science 337, 975–980 (2012). [PubMed: 22923583]
49. Slawson C & Hart GW O-GlcNAc signalling: implications for cancer cell biology. Nat Rev Cancer 11, 678–684 (2011). [PubMed: 21850036]
50. Yan Z et al. Structure of the rabbit ryanodine receptor RyR1 at near-atomic resolution. Nature 517, 50–55 (2015). [PubMed: 25517095]
51. Ruan HB et al. Calcium-dependent O-GlcNAc signaling drives liver autophagy in adaptation to starvation. Genes Dev 31, 1655–1665 (2017). [PubMed: 28903979]
52. Zou L et al. The Identification of a Novel Calcium-Dependent Link Between NAD(+) and Glucose Deprivation-Induced Increases in Protein O-GlcNAcylation and ER Stress. Front Mol Biosci 8, 780865 (2021). [PubMed: 34950703]
53. Favier FB, Britto FA, Freyssenet DG, Bigard XA & Benoit H HIF-1-driven skeletal muscle adaptations to chronic hypoxia: molecular insights into muscle physiology. Cell Mol Life Sci 72, 4681–4696 (2015). [PubMed: 26298291]
54. Cai D et al. IKKbeta/NF-kappaB activation causes severe muscle wasting in mice. Cell 119, 285–298 (2004). [PubMed: 15479644]
55. Wani WY, Chatham JC, Darley-Usmar V, McMahon LL & Zhang J O-GlcNAcylation and neurodegeneration. Brain Res Bull 133, 80–87 (2017). [PubMed: 27497832]
56. Lon HK et al. Pharmacokinetics, Safety, Tolerability, and Pharmacodynamics of Alicapistat, a Selective Inhibitor of Human Calpains 1 and 2 for the Treatment of Alzheimer Disease: An Overview of Phase 1 Studies. Clin Pharmacol Drug Dev 8, 290–303 (2019). [PubMed: 30052328]

57. Tsuyada A et al. CCL2 mediates cross-talk between cancer cells and stromal fibroblasts that regulates breast cancer stem cells. Cancer Res 72, 2768–2779 (2012). [PubMed: 22472119]
58. Ran FA et al. Genome engineering using the CRISPR-Cas9 system. Nat Protoc 8, 2281–2308 (2013). [PubMed: 24157548]
59. Shin HR et al. Small-molecule inhibitors of histone deacetylase improve CRISPR-based adenine base editing. Nucleic Acids Res 49, 2390–2399 (2021). [PubMed: 33544854]
60. Kim S, Bae T, Hwang J & Kim JS Rescue of high-specificity Cas9 variants using sgRNAs with matched 5' nucleotides. Genome Biol 18, 218 (2017). [PubMed: 29141659]
61. Gray JT & Zolotukhin S Design and construction of functional AAV vectors. Methods Mol Biol 807, 25–46 (2011). [PubMed: 22034025]
62. Sato K, Pollock N & Stowell KM Functional studies of RYR1 mutations in the skeletal muscle ryanodine receptor using human RYR1 complementary DNA. Anesthesiology 112, 1350–1354 (2010). [PubMed: 20461000]
63. Yan W et al. Cancer-cell-secreted exosomal miR-105 promotes tumour growth through the MYC-dependent metabolic reprogramming of stromal cells. Nat Cell Biol 20, 597–609 (2018). [PubMed: 29662176]
64. Stoner SA et al. High sensitivity flow cytometry of membrane vesicles. Cytometry. Part A : the journal of the International Society for Analytical Cytology 89, 196–206 (2016). [PubMed: 26484737]
65. Thery C et al. Minimal information for studies of extracellular vesicles 2018 (MISEV2018): a position statement of the International Society for Extracellular Vesicles and update of the MISEV2014 guidelines. J Extracell Vesicles 7, 1535750 (2018). [PubMed: 30637094]
66. Lim KL et al. Parkin mediates nonclassical, proteasomal-independent ubiquitination of synphilin-1: implications for Lewy body formation. J Neurosci 25, 2002–2009 (2005). [PubMed: 15728840]
67. Stephens J et al. Functional analysis of RYR1 variants linked to malignant hyperthermia. Temperature (Austin) 3, 328–339 (2016). [PubMed: 27857962]
68. Shevchenko A, Wilm M, Vorm O & Mann M Mass spectrometric sequencing of proteins silver-stained polyacrylamide gels. Anal Chem 68, 850–858 (1996). [PubMed: 8779443]
69. DeBalsi KL et al. Targeted metabolomics connects thioredoxin-interacting protein (TXNIP) to mitochondrial fuel selection and regulation of specific oxidoreductase enzymes in skeletal muscle. J Biol Chem 289, 8106–8120 (2014). [PubMed: 24482226]
70. Deacon RM Measuring the strength of mice. J Vis Exp (2013).
71. Svensson K et al. Combined overexpression of SIRT1 and knockout of GCN5 in adult skeletal muscle does not affect glucose homeostasis or exercise performance in mice. Am J Physiol Endocrinol Metab 318, E145–E151 (2020). [PubMed: 31794263]

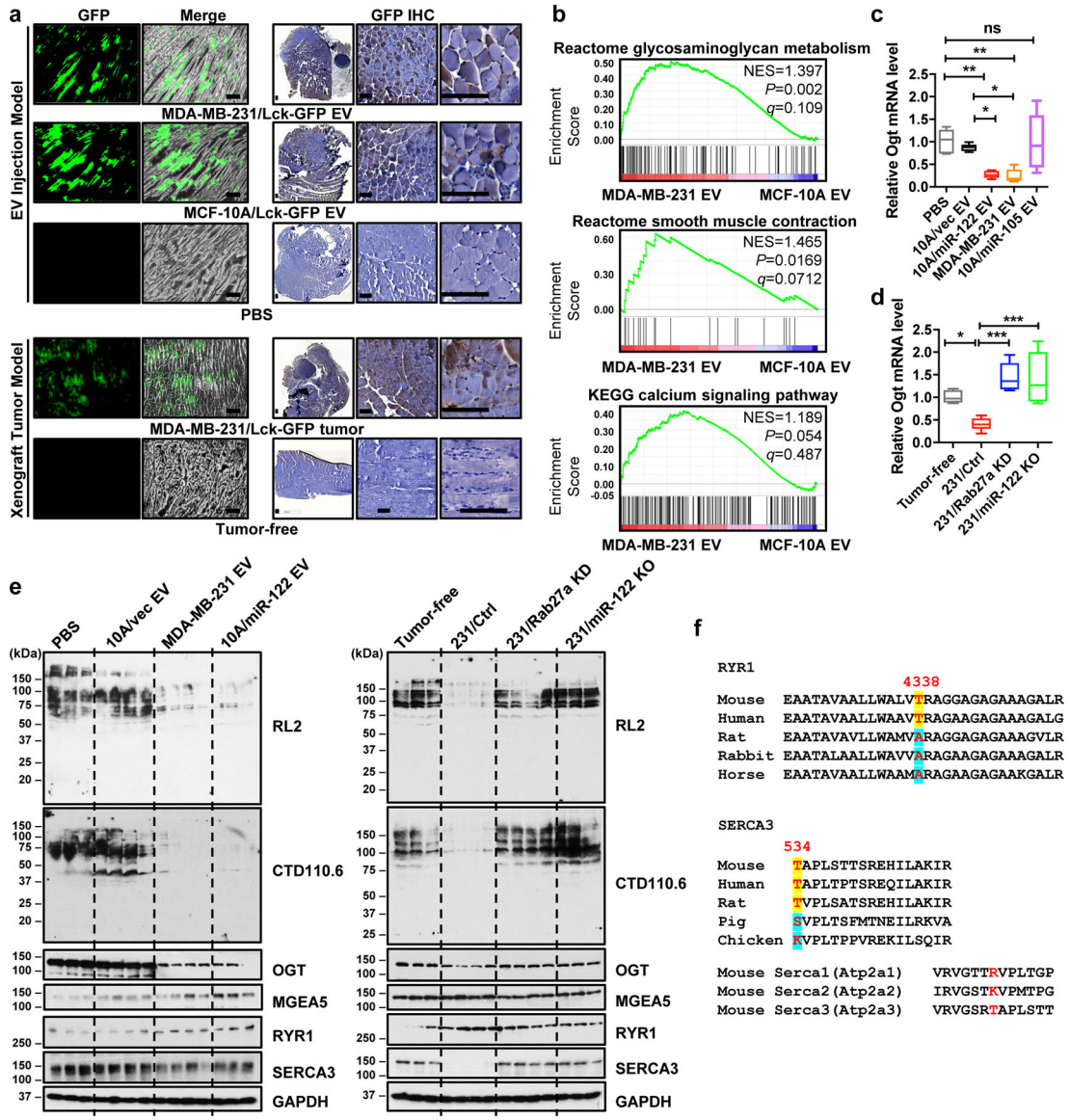

Figure 1: Cancer-secreted EVs suppress *O*-GlcNAcylation in skeletal muscle through miR-122.

(a) GFP signals in GA from NSG mice receiving tail vein injections of Lck-GFP-labelled EVs or bearing MDA-MB-231/Lck-GFP tumours. Left: GFP fluorescence (green) in longitudinal muscle sections. Right: Immunohistochemistry of GFP (brown) in muscle sections. Scale bar=100 μm. **(b)** GA collected from mice that had received MCF-10A- or MDA-MB-231-derived EVs for 5 weeks were subjected to RNA-seq and GSEA, showing enrichment of genes related to indicated pathways (n=4 mice for MCF-10A EVs and n=5 mice for MDA-MB-231 EVs). NES: normalized enrichment score. Nominal p-values and false discovery rate (FDR) q-values are shown. **(c,d)** RT-qPCR showing relative *Ogt* mRNA levels in GA of mice receiving indicated EVs (c) or bearing MDA-MB-231 tumours (d). Data were normalized to 18S rRNA and compared to the first group (one-way ANOVA with Tukey's multiple comparisons test, n=6 mice per group). The boxes in the box-and-whiskers plots show the median (centre line) and the quartile range (25–75%), and the whiskers

extend from the quartile to the minimum and maximum values. **(e)** Western blots showing levels of *O*-GlcNAcylation (by *O*-GlcNAc antibodies RL2 and CTD110.6) and indicated proteins in GA of indicated groups of mice. **(f)** MS-identified *O*-GlcNAcylation sites in mouse RYR1 and SERCA3, as well as the corresponding sequences in other species and in mouse SERCA1/2. *P<0.05, **P<0.01, ***P<0.001, ns: not significant. Unprocessed original scans of blots are shown in Extended Data.

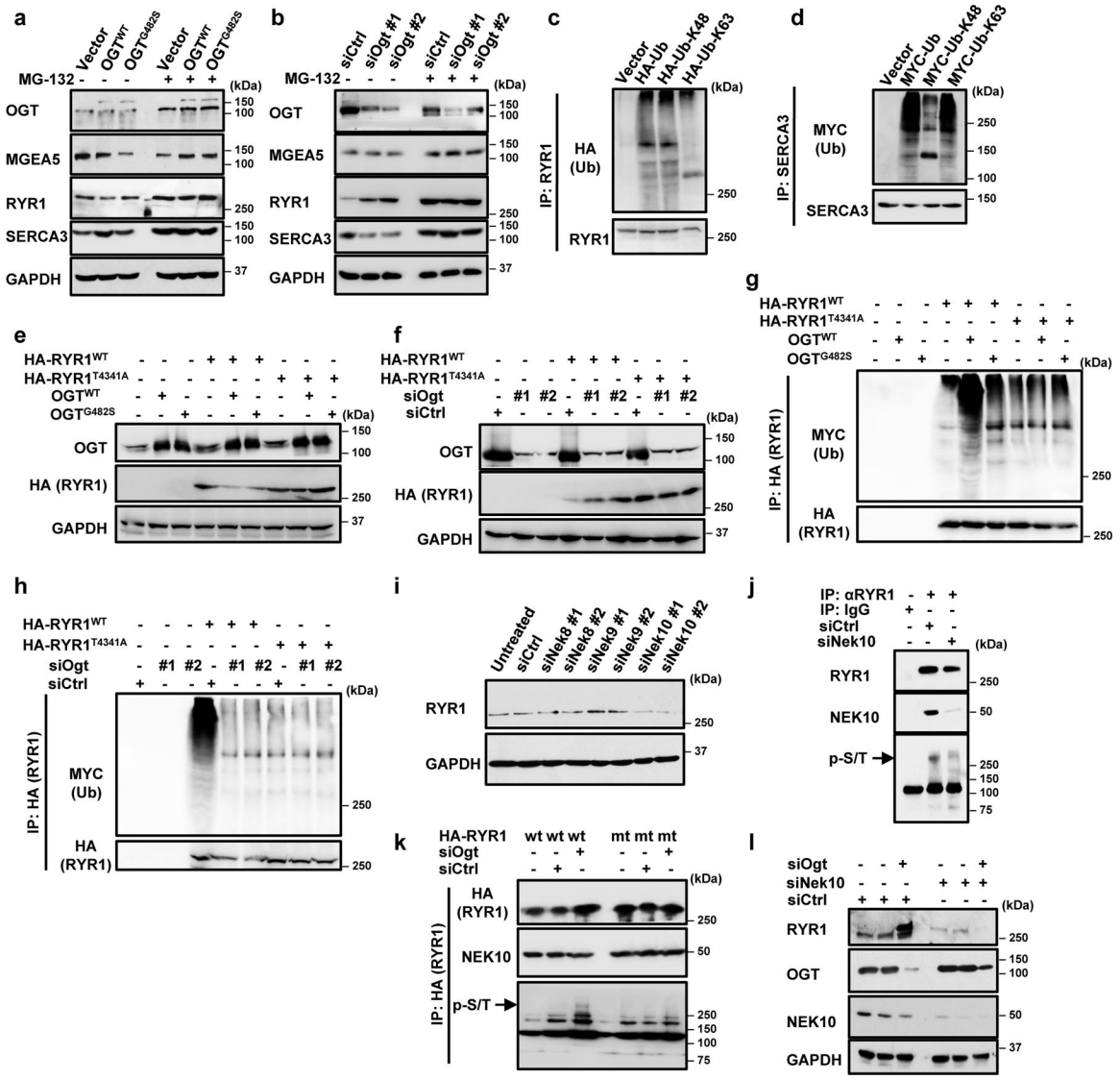

Figure 2: *O*-GlcNAcylation increases RYR1 ubiquitination and proteasomal degradation.

(a,b) Western blots showing indicated proteins in C2C12 myotubes with plasmid-directed overexpression of wild-type human OGT or an enzymatic dead mutant G482S (a), or with siRNA-mediated knockdown of OGT (b). Myotubes differentiated from transfected myoblasts were treated in the absence or presence of 10 μM proteasome inhibitor MG-132 for 12 h before the analysis. **(c,d)** Ubiquitination of endogenous RYR1 (c) and SERCA3 (d) detected in C2C12 myotubes expressing tagged ubiquitin (wild-type or mutants that only allow K48- or K63-linked ubiquitination). **(e,f)** Western blots of C2C12 myotubes expressing wild-type human RYR1 or T4341A mutant as well as indicated OGT expression plasmids (e) or OGT siRNA (f). **(g,h)** RYR1 ubiquitination detected by IP of tagged RYR1 followed by western blot of tagged ubiquitin (expressed from a plasmid). C2C12 myotubes with exogenous expression of wild-type or T4341A mutant of human RYR1 under OGT overexpression (g) or knockdown (h) were treated with 10 μM MG-132 for 12 h before lysates were prepared for IP. **(i)** RYR1 protein levels in C2C12 myotubes expressing

indicated siRNAs. **(j)** IP of endogenous RYR1 showing its interaction with NEK10, its serine/threonine phosphorylation, and the effect of NEK10 knockdown in C2C12 myotubes. **(k)** IP of exogenously expressed RYR1 (wild-type or T4341A mutant) showing the effect of OGT knockdown on its interaction with NEK10 and phosphorylation. **(l)** Levels of indicated proteins under OGT and NEK10 gene knockdown. Unprocessed original scans of blots are shown in Extended Data.

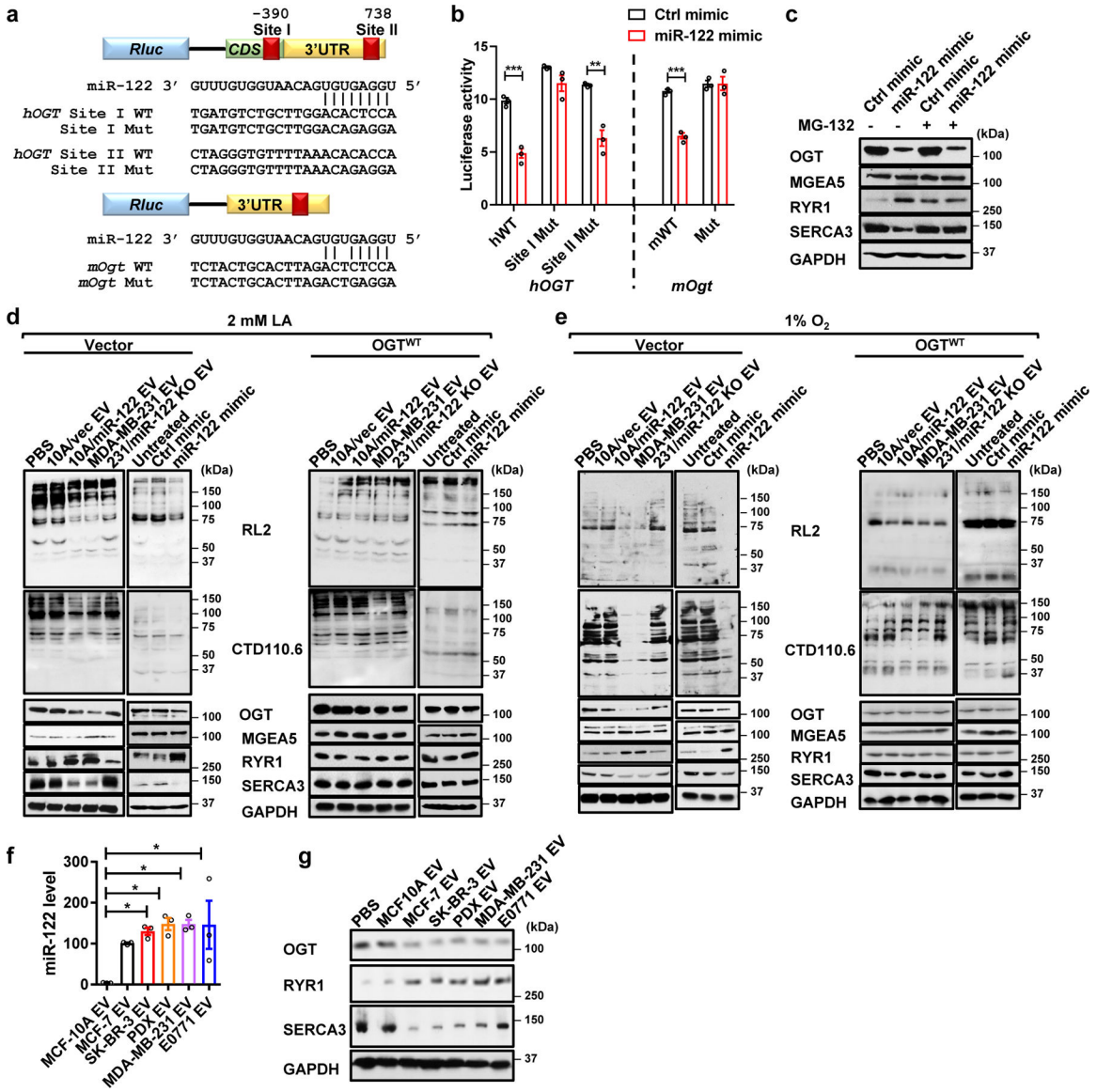

Figure 3: miR-122 regulates RYR1 and SERCA3 by directly targeting OGT.

(a) Predicted miR-122 binding sites in human and mouse *OGT/Ogt* genes. The corresponding sequences in wild-type (WT) and mutated reporters are shown. **(b)** Responsiveness of the reporters to miR-122 mimic in transfected C2C12 (unpaired two-tailed t-test, n=3 biological replicates). **(c)** Western blot showing levels of indicated proteins in C2C12 transfected with miR-122 or control mimic and grown in 2 mM lactate with or without MG-132 treatment. **(d,e)** Protein levels in C2C12 treated as indicated and grown in 2 mM lactate (d) or under 1% O_2 (e) with or without expression of exogenous wild-type OGT. **(f)** RT-qPCR-determined miR-122 levels in an equal amount of EVs from indicated cells (normalized to a synthetic cel-miR-39–3p spike-in control) (one-way ANOVA with Tukey's multiple comparisons test, n=3 biological replicates). **(g)** Protein levels in C2C12 treated with PBS or indicated EVs and grown in 2 mM lactate. In bar graphs, values are

shown as mean ± SEM. *P<0.05, **P<0.01, ***P<0.001. Unprocessed original scans of blots are shown in Extended Data.

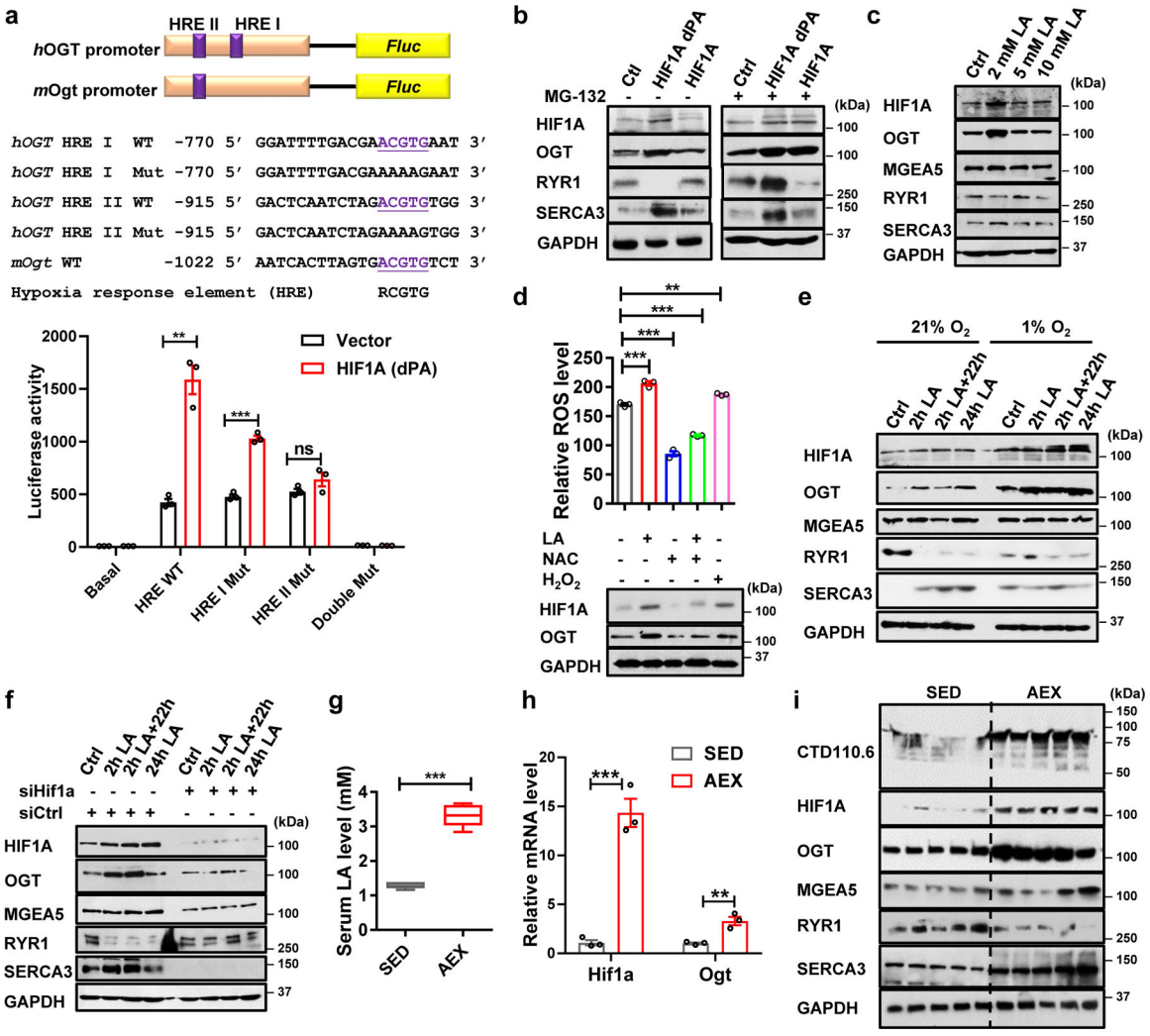

Figure 4: OGT expression is induced by lactate and hypoxia through HIF1A activation.

(a) A schematic of human and mouse *OGT/Ogt* genes showing putative hypoxia response elements (HREs) in the promoter region and the corresponding sequences in wild-type and mutated reporters. The nucleotide sequence is numbered in relation to the transcription start site, which is designated as +1. Lower panel: Luciferase reporter assay showing responsiveness of the reporters to transfected HIF1A (dPA) in C2C12 (unpaired two-tailed t-test, n=3 biological replicates). **(b)** Western blots showing indicated proteins in C2C12 transfected with wild-type HIF1A or the dPA mutant and with or without MG-132 treatment. **(c)** Protein levels in C2C12 myotubes grown under indicated concentrations of lactate (LA) for 24 h. **(d)** Relative levels of ROS and indicated proteins in C2C12 myotubes treated with 2 mM LA for 12 h with or without N-acetylcysteine (NAC; 5 mM for 1 h before harvesting cells) or treated with H_2O_2 (as a control; 1 mM for 6 h) (one-way ANOVA with Tukey's multiple comparisons test, n=3 biological replicates). **(e)** Protein levels in C2C12 treated with 2 mM LA (for 2 h, for 2 h followed by 22 h of incubation in LA-free medium, or for 24 h) and cultured under 21% or 1% O_2. **(f)** Protein levels in C2C12 treated as indicated and transfected with control siRNA or siRNA targeting HIF1A. **(g-i)** Levels of

serum LA (g; unpaired two-tailed t-test, n=5 mice per group) and indicated mRNA (h; unpaired two-tailed t-test, n=3 mice per group) and protein levels (i) in GA from female C57BL/6J mice collected immediately following 1 h of high-intensity treadmill running (aerobic exercise/AEX) or under sedentary lifestyle (SED). In bar graphs, values are shown as mean ± SEM. The boxes in the box-and-whiskers plot show the median (centre line) and the quartile range (25–75%), and the whiskers extend from the quartile to the minimum and maximum values. $^{**}P<0.01$, $^{***}P<0.001$, ns: not significant. Unprocessed original scans of blots are shown in Extended Data.

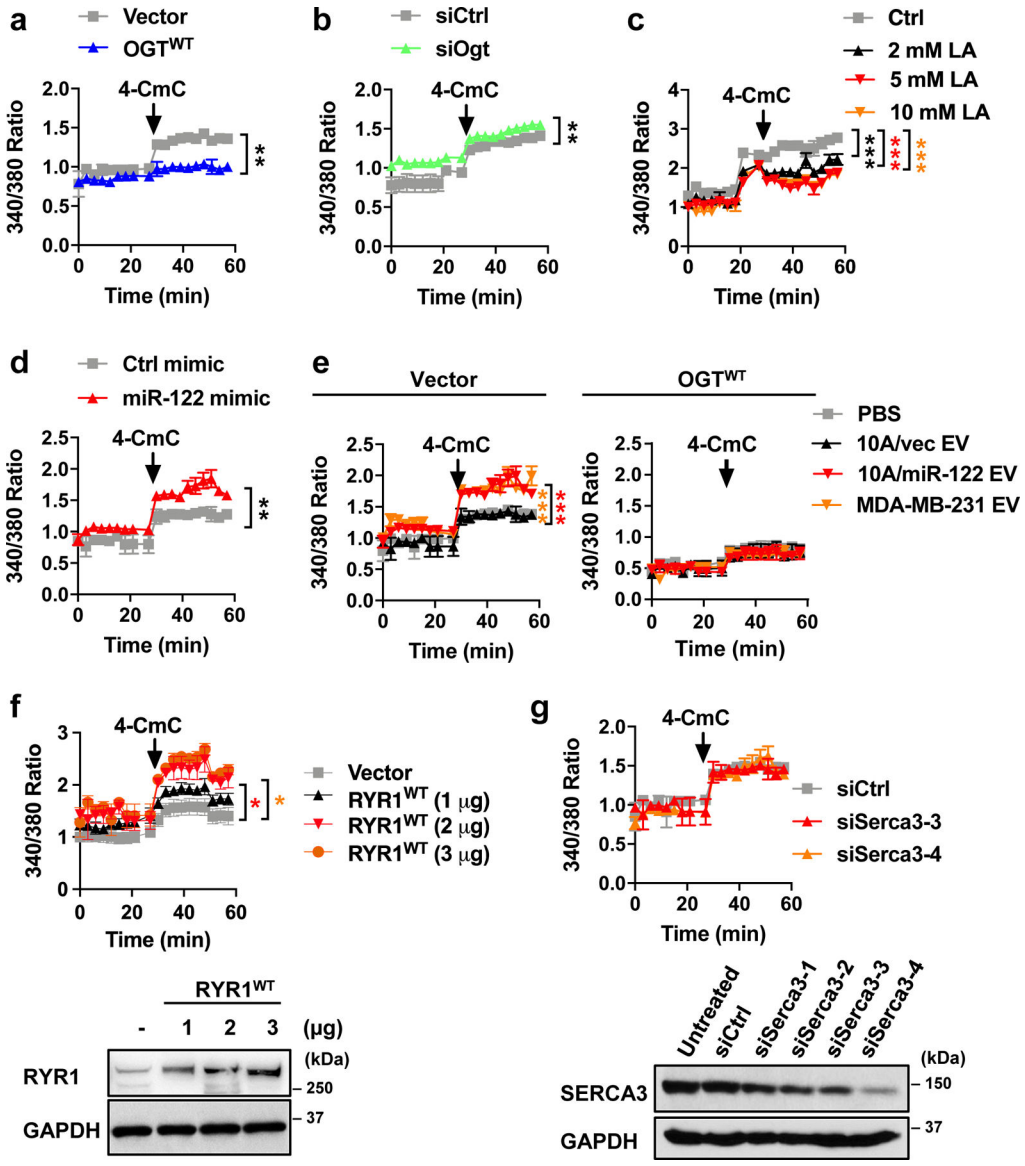

Figure 5: Cytosolic Ca^{2+} level is regulated by the miR-122–OGT–RYR1 axis.

Intracellular Ca^{2+} dynamics was measured in C2C12 myotubes loaded with Fura-2 AM. To stimulate Ca^{2+} release, 4-CmC was added at 500 μM. Treatments of C2C12 are as indicated, including overexpression of exogenous OGT (a), OGT gene knockdown (b), various concentrations of LA (c), transfection of miR-122 or control mimic (d), EV treatment with or without expression of exogenous OGT (e), expression of exogenous wild-type RYR1 by transfecting indicated amount of plasmid DNA (f), and SERCA3 gene knockdown (g). In line graphs, values are shown as mean ± SEM. Repeated measure two-way ANOVA with Bonferroni's multiple comparisons test was performed in a, b, and d, whereas repeated measure two-way ANOVA with Tukey's multiple comparisons test was performed in c, e-g (n=3 biological replicates for all panels). *P<0.05, **P<0.01, ***P<0.0001 comparing to the first group (grey curve). Unprocessed original scans of blots are shown in Extended Data.

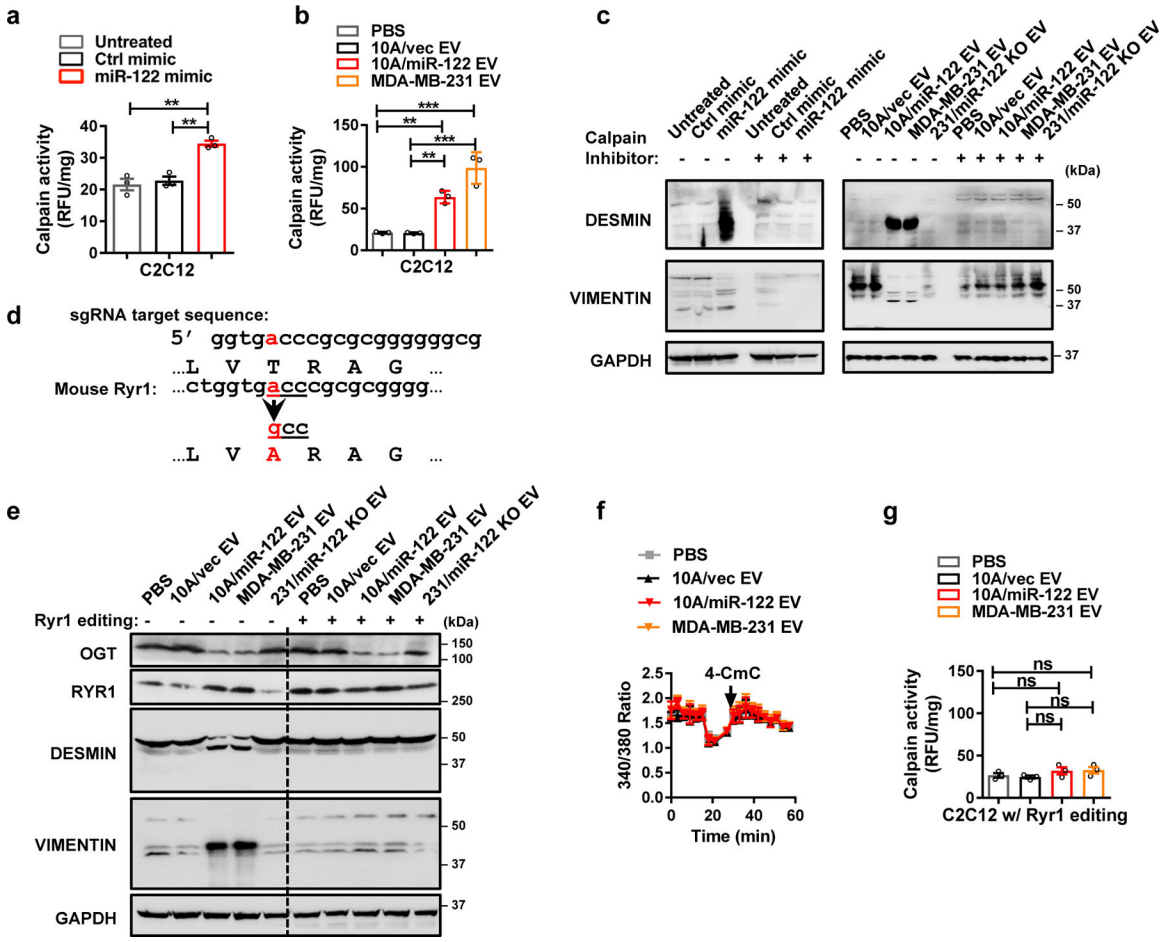

Figure 6: BC-secreted miR-122 induces calpain activity and protein cleavage in myotubes through regulating RYR1.

(a,b) Calpain protease activity measured in C2C12 myotubes treated as indicated (one-way ANOVA with Tukey's multiple comparisons test, n=3 biological replicates). **(c)** Western blots showing cleavage of indicated proteins in C2C12 myotubes with or without treatment with 50 nM Alicapistat (ABT-957) for 12 h. **(d)** A schematic showing targeted mutagenesis of endogenous mouse Ryr1 using an ABE-based system. The target DNA sequence of sgRNA used to introduce T4338A mutation is shown. **(e-g)** Western blots (e), intracellular Ca^{2+} dynamics (f; repeated measure two-way ANOVA with Tukey's multiple comparisons test, no significance found, n=3 biological replicates), and calpain protease activity (g; one-way ANOVA with Tukey's multiple comparisons test, n=3 biological replicates) measured in C2C12 myotubes with T4338A Ryr1 editing. In all bar and line graphs, values are shown as mean ± SEM. $^{**}P<0.01$, $^{***}P<0.0001$, ns: not significant. Unprocessed original scans of blots are shown in Extended Data.

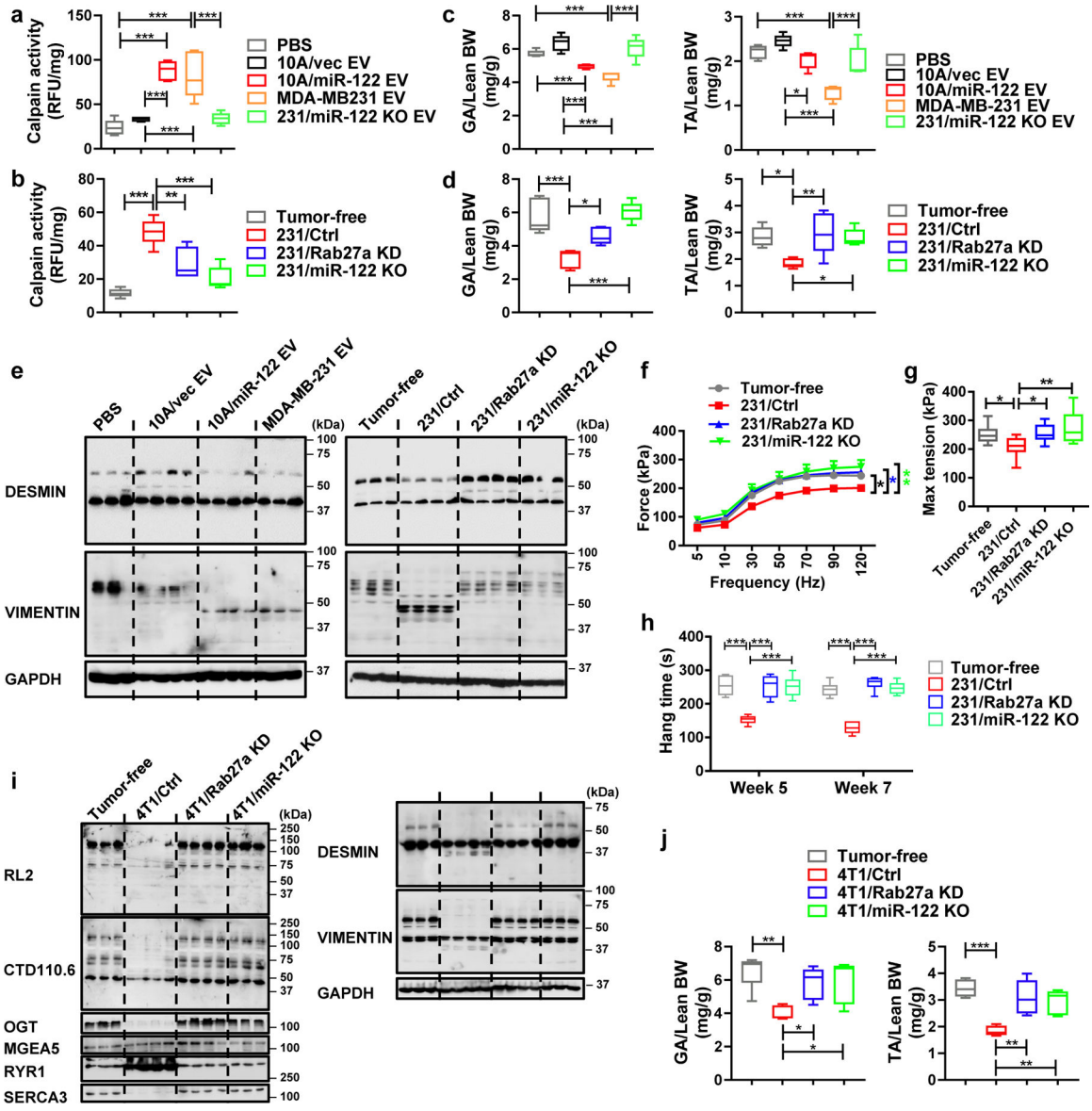

Figure 7: Regulation of calpain activity and protein cleavage in skeletal muscle by tumour-derived EVs.

(a,b) Calpain protease activity measured in GA of mice receiving EV treatments (a; n=5 mice per group) or bearing indicated tumours (b; n=5 mice per group) as those in Figure 1e (one-way ANOVA with Tukey's multiple comparisons test). **(c,d)** Skeletal muscle weight in indicated mouse groups (one-way ANOVA with Tukey's multiple comparisons test, n=5 mice per group). For tumour-bearing mice, muscle was analysed when tumours reached ~300 mm^3 in all groups. **(e)** Western blots showing cleavage of indicated proteins in GA of EV-treated or tumour-bearing mice. **(f)** Force-frequency curves normalized to maximum (repeated measure two-way ANOVA with Tukey's multiple comparisons test) and **(g)** maximum tetanic tension (one-way ANOVA with Tukey's multiple comparisons test) in the EDL from indicated tumour-free or tumour-bearing mice when tumours reached ~300 mm^3 (n=13 mice for tumour-free group, n=12 for 231/Ctrl group, n=8 for 231/Rab27a KD group,

and n=6 for 231/miR-122 KO group). **(h)** Inverted screen hang time tests in tumour-free and tumour-bearing NSG mice at week 5 and 7 after BC cell implantation (one-way ANOVA with Tukey's multiple comparisons test, n=6 mice per group). **(i)** Western blots of GA from female BALB/c mice bearing 4T1-derived tumours with tumour-free mice as controls. **(j)** Skeletal muscle weight in indicated mouse groups (one-way ANOVA with Tukey's multiple comparisons test, n=5 mice per group). In f, values are shown as mean ± SEM. The boxes in the box-and-whiskers plots show the median (centre line) and the quartile range (25–75%), and the whiskers extend from the quartile to the minimum and maximum values. *P<0.05, **P<0.01, ***P<0.001. Unprocessed original scans of blots are shown in Extended Data.

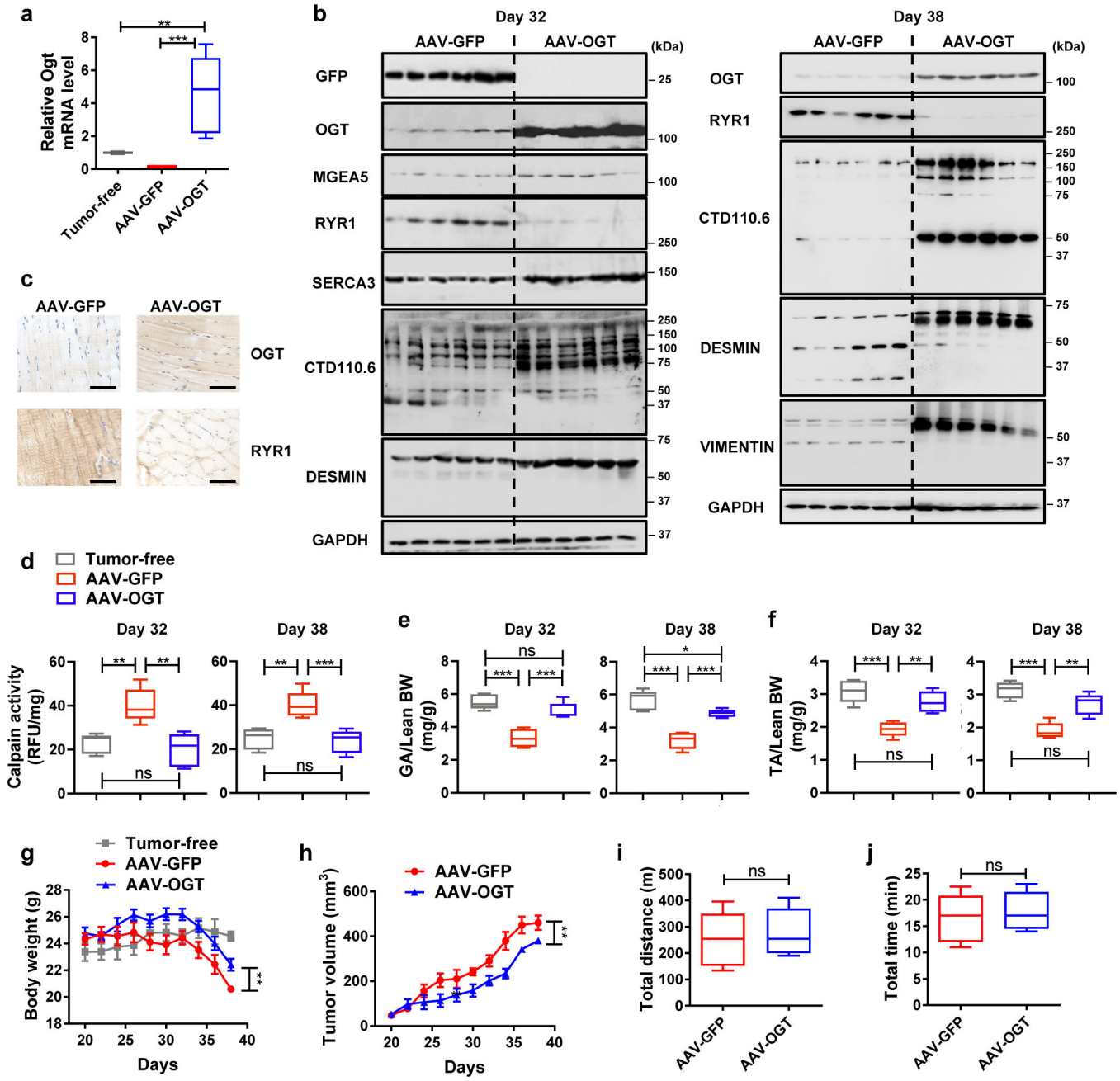

Figure 8: Exogenous OGT expression alleviates BC-associated proteolysis and skeletal muscle loss.

AAV-OGT virus or AAV-GFP control virus were injected into GA and TA of both sides one week after implantation of MDA-MB-231 cells. Organs were collected on day 38 (or as indicated on both day 32 and 38) after implantation. **(a-d)** *Ogt* mRNA levels (a; one-way ANOVA with Tukey's multiple comparisons test, n=6 mice per group), western blots (b), IHC of OGT and RYR1 (c; bar=100 μm), and calpain protease activity (d; one-way ANOVA with Tukey's multiple comparisons test, n=5 mice per group) in GA. **(e,f)** GA and TA were weighed and normalized to lean body mass (one-way ANOVA with Tukey's multiple comparisons test, n=5 mice per group). **(g)** Body weight followed in all mouse

groups (repeated measure two-way ANOVA with Tukey's multiple comparisons test, n=6 mice per group). **(h)** Tumour volume followed in tumour-bearing mice (repeated measure two-way ANOVA with Bonferroni's multiple comparisons test, n=6 mice per group). **(i,j)** Total running distance (i) and time (j) measured in week 5 in a run-to-exhaustion treadmill test (unpaired two-tailed t-test, n=5 mice per group). In g and h, values are shown as mean ± SEM. The boxes in the box-and-whiskers plots show the median (centre line) and the quartile range (25–75%), and the whiskers extend from the quartile to the minimum and maximum values. *P<0.05, **P<0.01, ***P<0.001, ns: not significant. Unprocessed original scans of blots are shown in Extended Data.